ADVANCING EARTH AND SPACE SCIENCE

JGR Space Physics

RESEARCH ARTICLE
10.1029/2021JA030247

Key Points:

- Global-scale storm-induced electron density responses are studied during boreal/austral summer storms, as well as equinoctial month storm
- Temporal lags and interhemispheric asymmetries are observed in electron density perturbations during boreal and austral summer storms
- These results are consistent with differences in the AMPERE interhemispheric field-aligned currents

Correspondence to:
N. Swarnalingam,
nimalan.swarnalingam@nasa.gov

Citation:
Swarnalingam, N., Wu, D. L., & Gopalswamy, N. (2022). Interhemispheric asymmetries in ionospheric electron density responses during geomagnetic storms: A study using space-based and ground-based GNSS and AMPERE observations. *Journal of Geophysical Research: Space Physics*, *127*, e2021JA030247. https://doi.org/10.1029/2021JA030247

Received 27 DEC 2021
Accepted 13 APR 2022

Interhemispheric Asymmetries in Ionospheric Electron Density Responses During Geomagnetic Storms: A Study Using Space-Based and Ground-Based GNSS and AMPERE Observations

N. Swarnalingam[1,2], D. L. Wu[1], and N. Gopalswamy[1]

[1]NASA Goddard Space Flight Center, Greenbelt, MD, USA, [2]Department of Physics, Catholic University of America, Washington, DC, USA

Abstract We utilize Total Electron Content (TEC) measurements and electron density (Ne) retrieval profiles from Global Navigation Satellite System (GNSS) receivers onboard multiple Low Earth Orbit (LEO) satellites to characterize large-scale ionosphere-thermosphere system responses during geomagnetic storms. We also analyze TEC measurements from GNSS receivers in a worldwide ground-based network. Measurements from four storms during June and July 2012 (boreal summer months), December 2015 (austral summer month), and March 2015 (equinoctial month) are analyzed to study global ionospheric responses and the interhemispheric asymmetry of these responses. We find that the space-based and ground-based TECs and their responses are consistent in all four geomagnetic storms. The global 3D view from GNSS-Radio Occultation (RO) Ne observations captures enhancements and the uplifting of Ne structures at high latitudes during the initial and main phases. Subsequently, Ne depletion occurs at high latitudes and starts progressing into midlatitude and low latitude as the storm reaches its recovery phase. A clear time lag is evident in the storm-induced Ne perturbations at high latitudes between the summer and winter hemispheres. The interhemispheric asymmetry in TEC and Ne appears to be consistent with the magnitudes of the Active Magnetosphere and Planetary Electrodynamics Response Experiment (AMPERE) high latitude integrated field-aligned currents (FACs), which are 3–4 MA higher in the summer hemisphere than in the winter hemisphere during these storms. The ionospheric TEC and Ne responses combined with the AMPERE-observed FACs indicate that summer preconditioning in the ionosphere-thermosphere system plays a key role in the interhemispheric asymmetric storm responses.

1. Introduction

Solar energy is transferred to the Earth's upper atmosphere primarily by two channels. In the first case, solar radiation is directly absorbed by the sunlit upper atmosphere. In the second case, energy is transferred to the polar upper atmosphere via the interaction between the solar wind and Earth's magnetic field, in which the absorbed energy is transferred in the forms of precipitated particles, electric fields, and currents. Although little energy is normally transferred to the polar upper atmosphere in geomagnetically quiet times, significant amounts of energy are transferred occasionally during highly disturbed geomagnetic conditions—geomagnetic storms. The most intense geomagnetic storms are mainly caused by Earth-directed Coronal Mass Ejections (CMEs; e.g., Gopalswamy, 2010; Tsurutani et al., 2006). Although the solar cycle strength may vary from one cycle to another and the number and frequency of storms are also reduced in weak cycles due to the reduction in the number of fast and wide CMEs and their magnetic content, studies show that the efficiency of the process causing geomagnetic storms has not changed significantly between the cycles (Gopalswamy, Tsurutani et al., 2015, Gopalswamy et al., 2020). Geomagnetic storms have attracted a large amount of attention since they can seriously affect not only satellites, aviation, and navigation and communication systems but also electrical power grids and oil and gas pipelines on the ground.

The Disturbance Storm Time (Dst) index is a measure of the intensity of geomagnetic storms, and its temporal profile during a storm is divided into initial, main, and recovery phases (Sugiura, 1964). A storm generally begins with an increase in the Dst index to positive values known as Sudden Impulse (SI) or Storm Sudden Commencement (SSC), which signals the arrival of the interplanetary shock structure on the dayside of the Earth's magnetopause (e.g., Gonzalez et al., 1994). This feature generally coincides with the initial phase in which

Earth's magnetopause experiences increased dynamic ram pressure from the solar wind (Tsurutani et al., 2006). SSC is followed by the main phase of the storm. During the main phase, as high energetic particle injection and energization build up an intensified partial ring current, strong magnetic fields opposite to the Earth's field are induced. These magnetic fields cause a rapid decrease in the Earth's magnetic field, especially in the equatorial and low-latitude regions, which is characterized by the Dst index. The Dst index continues to decrease and reaches a minimum value at the end of the main phase. The Dst then slowly returns to normal conditions during the recovery phase. While the initial and main phases last for hours, the recovery phase can last for several days.

During the storm phases, variability in the ionosphere-thermosphere system, which is normally dominated by lower atmospheric drivers, are either partially or fully dominated by the interaction between the solar wind and the magnetosphere and hence their coupling. As planetary magnetic disturbances continue, particle precipitation and field-aligned currents (FACs) that connect the auroral ionosphere with the outer magnetosphere are intensified, leading to increases in ionization, Joule heating, and density perturbation in polar regions that subsequently enhance convection patterns, changes in wind circulation, the generation of Storm Enhanced Density (SED; Foster, 1993) patches, and even modifications in the composition of the neutral gas (e.g., Förster & Jakowski, 2000; Fuller-Rowell et al., 1997; Pfaff, 2012; Prölss, 1997, and references therein). Disturbances at high latitudes might trigger Traveling Ionospheric Disturbances (TIDs; Hunsucker, 1982), which are propagating perturbations in the ionosphere and can be felt at almost all latitudes (Balthazor & Moffett, 1997). Disturbances at high latitudes might also generate disturbance winds and hence the Disturbance Dynamo Electric Fields (DDEFs) that are experienced from subauroral to middle and low latitudes (e.g., Amory-Mazaudier et al., 2017; Klimenko & Klimenko, 2012; Lu et al., 2008; Richmond & Matsushita, 1975). Moreover, due to an imbalance between the region-1 and region-2 FACs, the so-called Prompt Penetration Electric Fields (PPEFs) may extend beyond the auroral oval to the equatorial region (e.g., Fejer et al., 1983; Spiro et al., 1988), resulting in an increased F-region plasma density at low latitudes closer to the magnetic equator (Abdu et al., 2012; Lu et al., 2012; Mannucci et al., 2005). In subauroral regions where electric conductivity is generally low, northward-directed disturbance electric fields potentially generate a Sub-Auroral Polarization Stream (SAPS; Foster & Burke, 2002) and lead to plumes (e.g., Coster & Foster, 2007; Foster & Vo, 2002). Over the years, several multifront studies at different spatial and temporal scales have led to improvements in the fundamental understanding of these effects (e.g., Balan et al., 2018; Greenspan et al., 1991; Tsurutani et al., 2004; Zhang et al., 2017; Zou et al., 2014, and references therein).

One of the primary components in the space weather environment surrounding Earth is changes in the ionospheric electron density (N_e) during geomagnetic storms. More importantly, the extent to which changes occur in the ionospheric N_e during geomagnetic storms is an important question in the Earth's surrounding space weather research. Recent advancements in the techniques of tracking the Global Navigation Satellite System (GNSS) using ground-based and space-based receivers have facilitated the monitoring of changes in ionospheric N_e globally (e.g., Coster & Skone, 2009; Mendillo, 2006); hence, they have become one of the standard methods for studying the effects of geomagnetic storms on the ionosphere (e.g., Astafyeva, 2009; Yizengaw et al., 2006). During the onset of a storm, the F-region ionospheric N_e either increases or decreases in different phases, leading to positive and negative ionospheric storms on global or regional scales (e.g., Horvath & Lovell, 2015; Mendillo, 1973). Storm-induced enhanced convection of electric fields and dynamo effects, large-scale changes in wind circulation, and TIDs are generally considered the major causes of positive storms (e.g., Balan et al., 2018; Lu et al., 2008; Mendillo, 2006; Prölss, 1997). On the other hand, modifications in the upper atmospheric neutral gas composition at high and subauroral latitudes due to enhanced Joule heating are generally considered major causes of the negative storm (Danilov, 2013; Fuller-Rowell et al., 1997; Immel & Mannucci, 2013; Meier et al., 2005; Prölss, 2011). Studies show that the spatiotemporal evolution of ionospheric N_e may vary considerably from one storm to another, indicating regional dependencies at least in equatorial and low-latitudinal regions (e.g., Astafyeva et al., 2015; Dashora et al., 2019; Maruyama et al., 2007). Questions arise as to whether hemispheric seasonality might influence storm responses, especially at high latitude and midlatitude, since the summer hemisphere would possibly have a high conductive ionosphere due to a higher rate of ionization. Earlier, Duncan (1969) noticed that a magnetic disturbance perturbs the high latitude F-region most strongly during summer compared to winter.

Motivated by the aforementioned results, we consider four geomagnetic storms to investigate and characterize the ionospheric N_e response and to explore the interhemispheric asymmetry focusing mainly at high latitude and midlatitude. The selected storms are caused by Interplanetary CMEs (ICMEs) and occurred in June and July 2012 (northern summer months), December 2015 (southern summer month), and March 2015 (equinoctial month). We focus on satellite observations of global morphology in storm-induced ionospheric perturbations. The new data and the recently increased satellite observations allow us to characterize and comprehend the interhemispheric asymmetry of ionospheric storm responses. The new data sets include upward-looking space-based Total Electron Content (TEC) measurements from GNSS receivers onboard multiple Low Earth Orbit (LEO) satellites, TEC measurements from the worldwide ground-based GNSS receiver network, and GNSS-Radio Occultation (RO) N_e measurements.

Following the description of the different types of data sets that are used in this study, Section 2 describes the analysis method and the handling of sampling effects to observe global ionospheric TEC and N_e responses during these four geomagnetic storms. The evolution of the four storms that occurred in the boreal and austral summer months, as well as in the equinoctial month, are discussed in Section 3. The observed interhemispheric ionospheric asymmetrical TEC and N_e responses, especially at high latitude and midlatitude, are discussed in detail in this section. In this analysis, we also incorporate high-latitude FACs measurements from Active Magnetosphere and Planetary Electrodynamics Response Experiment (AMPERE). The daytime and nighttime storm-induced TEC perturbation analyses are presented in Section 4. These results further support our findings. Finally, in Section 5, we summarize the observed consistency between the interhemispheric asymmetric N_e responses and AMPERE measurements of FACs in all four storms and discuss the possible effects of seasonal preconditions on the ionospheric responses during these storms.

2. Data Set and Methodology

We use upward-looking TEC measurements and GNSS-RO N_e profiles from multiple LEO satellites. While TEC measurements allow us to study the topside ionosphere and plasmasphere, GNSS-RO measurements establish N_e profiles below the orbital altitudes. In our study, we establish TEC and N_e measurements as functions of latitude and time to characterize ionospheric electron responses during geomagnetic storms. In addition, we also use TEC measurements from a large number of ground-based GNSS satellite receivers distributed worldwide such that they are capable of producing a high-resolution data set in space and time.

2.1. Satellite Data Set

The LEO satellites record TEC measurements along the line of sight with GNSS satellites using their Precise Orbit Determination (POD) antenna directed to GNSS satellites. Unlike GPS-RO antennas, onboard quasi-zenith directed GPS-POD antennas provide nonocculting TEC information from the orbital altitude of the LEO satellite to the orbital altitude of the GNSS (e.g., Pedatella et al., 2011; Schreiner et al., 1999). These measurements, namely, PODTEC, contain absolute TEC measurements from the LEO satellite to the GNSS satellite along the ray path called Slant TEC (STEC). STECs are then converted to equivalent vertical TEC (VTEC) using a mapping function, $M(\theta)$

$$VTEC = \frac{STEC}{M(\theta)} \tag{1}$$

where θ is the elevation angle of the slant ray path. For ground-based TEC conversion, several studies have been conducted to establish a proper mapping function by simplifying the Earth's ionosphere into a geometric model. A spherical shell of a thin ionospheric layer is generally assumed to surround the Earth at an effective altitude ~350–450 km above the Earth's surface (e.g., Lanyi & Roth, 1988; Mannucci et al., 1998)

$$M(\theta) = \frac{1}{\sqrt{1 - \left(\frac{R_e}{R_e + h_i}\right)^2 \cos^2(\theta)}}, \tag{2}$$

where h_i is the effective altitude of the ionosphere and R_e is the Earth's radius. However, in LEO satellites, since the orbital altitude is generally at or above the F2 region of the ionosphere, their effective altitude of the ionosphere is generally higher than the effective altitude of the ionosphere described above for the ground-based GNSS measurements. Therefore, in LEO-based TEC observations, the orbital altitude should be considered for the selection of the effective altitude of the ionosphere. In this case, the corresponding mapping function is generally defined as follows:

$$M(\theta) = \frac{1}{\sqrt{1 - \left(\frac{R_{orbit}}{R_{shell}}\right)^2 \cos^2(\theta)}}, \tag{3}$$

where R_{orbit} and R_{shell} are the geocentric distances of the LEO satellite orbit and spherical ionospheric shell, respectively (Klobuchar, 1996). On the other hand, Lear (1987) proposed the following empirical mapping function for LEO satellite GNSS receivers:

$$M(\theta) = \frac{2.037}{\sin(\theta) + \sqrt{1.076 - \cos^2(\theta)}}. \tag{4}$$

Although these mapping functions show a dependence on parameters such as orbital altitude, magnetic latitude, and solar activity, comparison studies show that their differences are indeed insignificant, especially for higher elevation angles (greater than ~40°; Zhong, 2016). In our case, the orbital altitudes for LEO satellites range from ~450 to ~830 km during the period of geomagnetic storms considered in this work. We decided to use the Lear mapping function to convert STEC measurements to equivalent VTECs and maintain consistency in our analysis. In addition, we only consider STEC measurements that have elevation angles higher than 40° to mitigate the error caused by the STEC to VTEC conversion.

In this study, we purely focus on experimental data sets. We use TEC observations from the Constellation Observing System for Meteorology, Ionosphere, and Climate (COSMIC-1), Gravity Recovery and Climate Experiment (GRACE), and Meteorological Operational Satellite Program of Europe (MetOp-A/B) missions for the four geomagnetic storms. As described above, these nonocculting TEC measurements are obtained from LEO satellite orbital altitudes to GNSS satellites. GRACE has two sun-synchronized satellites such that one follows the other at an altitude of ~450 km. MetOp-A/B missions are also sun-synchronized satellites, orbiting in a coplanar orbit approximately half an orbit apart at an altitude of ~830 km. On the other hand, the COSMIC-1 constellation has six circular orbit satellites at an altitude of ~800 km, and hence, it has a better spatial coverage than the others. We consider data collected a few days prior to and after the storms that we intend to study. The data were obtained through the COSMIC Data Analysis and Archive Center (CDAAC). We perform quality control checks on these preprocessed data, in particular for any sudden spikes or outliers, and remove them. If we notice any sudden jump or drop in the continuity, we fix these aberrations using the method described in a previous study (Horvath & Crozier, 2007). Nevertheless, these situations occurred <3% of the total length of time in the data. In addition, we discard any measurement that was already flagged by CDAAC for error.

Although satellite observations have uniform global coverage, they have limited spatial and temporal sampling. Most of the previous studies were performed using along the track TEC measurements. Since our focus is to characterize interhemispheric large-scale ionospheric N_e responses during geomagnetic storms, we bin the data into a 10° latitude by 20° longitude grid for each hour in universal time and then average along the longitude and time. Because satellite space and time sampling cause artifacts, we consider multiples of the satellite orbital time as the average time to minimize these effects in our analysis. For example, Figure 1 shows the GRACE latitude-time coverage during its upward-looking TEC measurements in March 2015. The upper panel shows the measured STECs in TEC units (1 TECU = 10^{16} m^{-2}) for five orbital cycles on 10 March, which was a quiet day, and the lower panel shows the same data on 17 March, which was a storm day. Furthermore, the TEC measurements with elevation angles smaller than 40° are marked in grayscale, and as noted above, those measurements are ignored in our analysis. As shown in this figure, the GRACE orbital time is ~90 min, and we consider 180 min of zonal averaging, which represents the combination of two orbital cycles. This approach allows us to conduct our analysis separately for daytime (06:00–18:00 local time) and nighttime (18:00–06:00 local time) to facilitate the analysis with a minimal or no data gap. As we will discuss shortly, the sampling artifacts are repeatable on a daily basis and can be removed using quiet-time daily variation of TECs.

In addition to TEC observations, we also utilize GNSS-RO N_e measurements from the COSMIC-1 and GRACE missions. The GNSS-RO receivers in these satellites record the carrier phase changes of the GNSS-to-LEO link during the rises and sets of GNSS satellites with respect to LEO satellites. These measurements are used

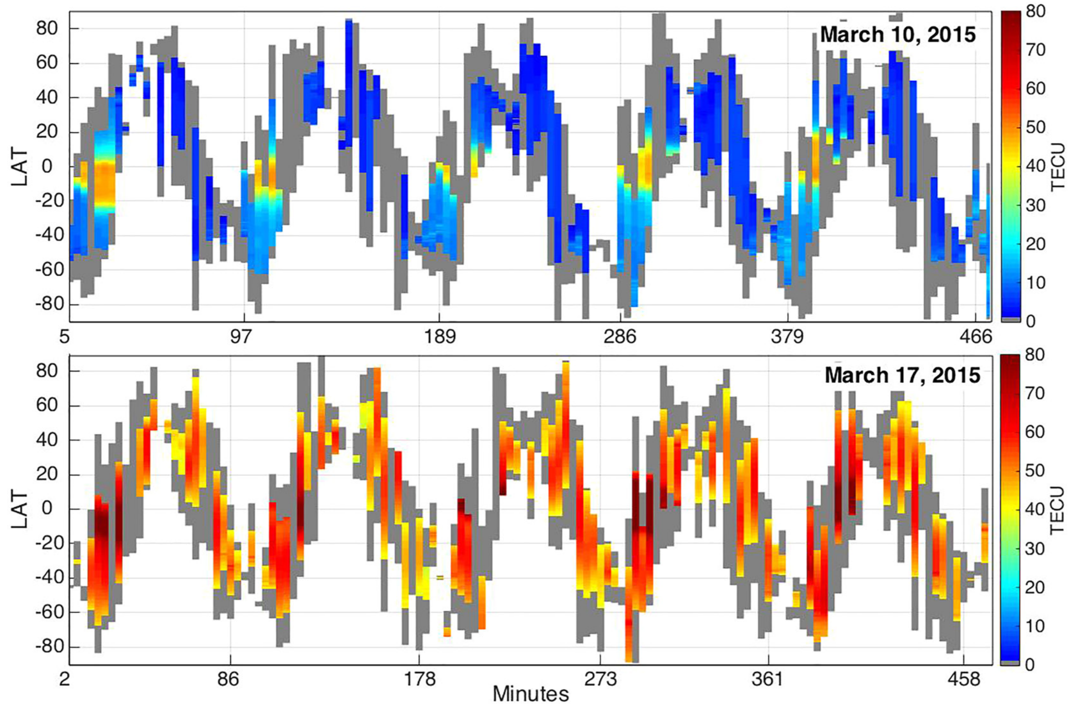

Figure 1. Latitude-time coverage of Gravity Recovery and Climate Experiment (GRACE) during its upward-looking Total Electron Content (TEC) measurements in March 2015. The measured Slant TECs (STECs) for five orbital cycles on 10 March (quiet day) and 17 March (storm day) are shown in the upper and lower panels, respectively. STEC measurements with elevation angles smaller than 40° are marked with a gray color scale.

in inversion techniques to compute N_e profiles of the ionosphere (e.g., Schreiner et al., 1999). N_e profiles are available from LEO orbital altitudes and down to ∼100 km. Unlike STEC measurements, GNSS-RO N_e measurements allow the investigation of ionospheric responses in three dimensions: altitude, latitude, and time. However, the number of available profiles is relatively low compared to STEC measurements. In the case of COSMIC-1, ∼1,000 profiles are available in a typical day requiring a 6-hr averaging to avoid gaps in the global N_e observations during storms. The GNSS-RO N_e are obtained using Abel inversion with the assumption of spherical symmetry, and previous studies documented systematic errors in the equatorial and low-latitudinal regions, especially at low altitudes (e.g., Liu et al., 2010; Yue et al., 2010). Although improvements have been implemented in recent years (e.g., Nicolls et al., 2009; Pedatella et al., 2015), the method still produces errors in the E-region (Swarnalingam et al., 2020; Wu, 2018). Nevertheless, this data set is a useful tool to explore large-scale N_e studies in the F-region (e.g., Pedatella et al., 2011). In this study, we use them above 200 km in parallel to TEC observations to characterize N_e responses during the progress of storms in the high-latitude and midlatitude regions.

2.2. Ground-Based Data Set

We also use another VTEC data set from global ground-based GNSS receivers that are collected and provided by the MIT Haystack Observatory via the CEDAR Madrigal system. The TEC data are collected on a daily basis from a large number of worldwide sites (∼6,000) that correspond to ∼100 million line-of-sight TEC measurements (Coster et al., 2017). Automated GNSS processing algorithms are used to convert these measurements to VTEC directly above each location (Rideout & Coster, 2006), with a special focus on removing any bias among receivers (Vierinen et al., 2016). Subsequently, the data are arranged into 1° latitude by 1° longitude bins and are archived every 5 min; hence, the data produce a good temporal resolution in TEC measurements. For example, Figure 2 compares the observed latitude-longitude VTEC at 16:35 UT on 10 March (quiet day) and 17 March (storm day) in 2015 along with the respective Dst indices. The sun position is marked with a yellow circle.

As illustrated in Figure 2, the ground-based GNSS receiver locations are not uniformly distributed and only cover landmass areas, leaving portions of oceans uncovered. Nevertheless, the ground-based TEC observations cover

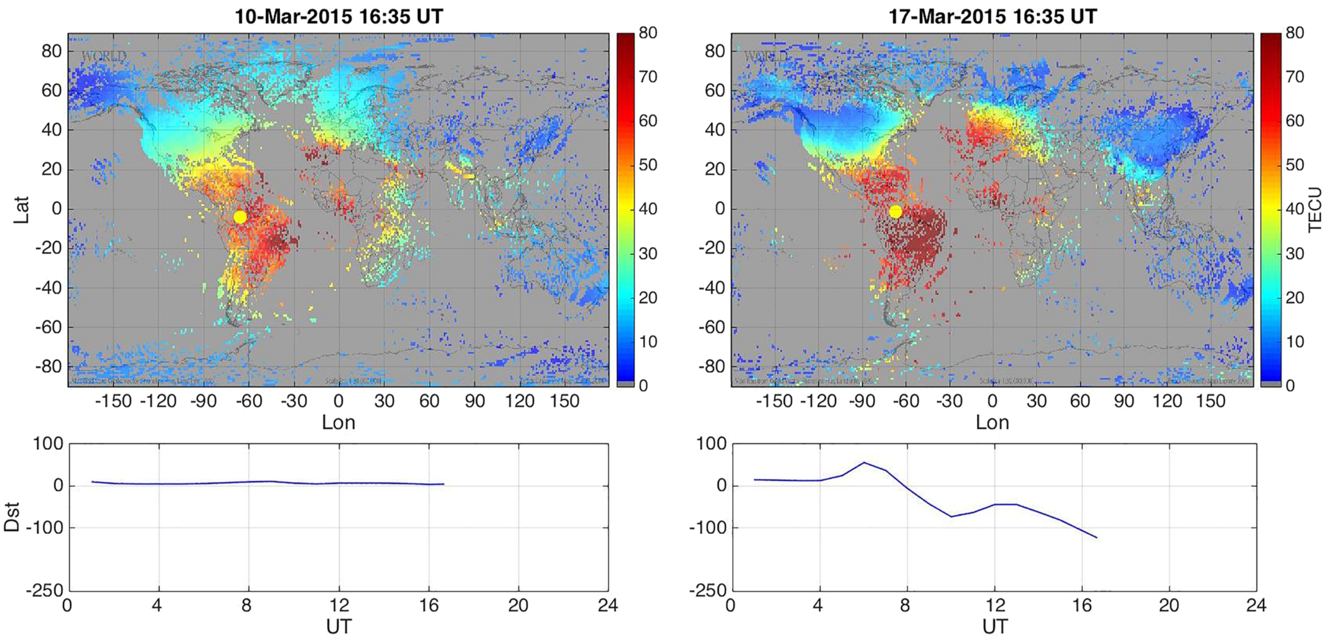

Figure 2. Comparisons of vertical TEC (VTEC) observations from the global ground-based Global Navigation Satellite System (GNSS) receivers on 10 March (quiet day) and 17 March (storm day) in 2015 along with the respective Dst indices are shown on the left and right, respectively. The sun position is marked with a yellow circle. A large number of global receiver locations covering Earth's landmass produce a high-resolution data set in space and time.

the entire ionosphere and plasmasphere up to the GNSS orbital altitude (~220,000 km). On the other hand, the space-based observations uniformly cover both landmass and ocean areas, but as described above, they have limited spatial and temporal sampling. In addition, the space-based TEC observations that we use in this study cover only the topside of the ionosphere from the orbital altitudes of the LEOs. Although these data products have their own positive and negative qualities, they provide promising insights into storm-induced ionospheric plasma effects. In our analysis method, even though these data produce sampling artifacts on the global scale, they are repeatable on a daily basis and hence can be removed using quiet-time daily variation, as we will briefly discuss in Section 4.

2.3. FACs

FACs connect the auroral ionosphere with the outer magnetosphere. They intensify during the onset of storms. However, they have not been studied extensively in association with storms. In this study, in addition to the space-based and ground-based GNSS TEC and GNSS-RO N_e data sets, we incorporate FACs. We use FAC estimations from the AMPERE during the four storms. The AMPERE determines FACs using transverse magnetic field measurements recorded by magnetometers on 66 communications satellites, orbiting at ~780 km and comprising the Iridium constellation (Anderson et al., 2000). From the measurements of magnetometers, magnetic perturbations are calculated every 10 min by subtracting the Earth's main field. Subsequently, FACs are determined from the spatial gradients of the vector magnetic field perturbations by considering the satellite altitude and instrument gain (Anderson et al., 2014). The accumulated measurements over 10 min are updated every 2 min for both hemispheres. In our analysis, we use upward and downward integrated FACs for magnetic latitudes poleward of 60° in the Northern and Southern Hemispheres during the onset of storms.

3. Asymmetric Ionosphere Electron Density Responses—Representative Examples

3.1. 14–15 July 2012 Storm

The 14–15 July 2012 event was an intense geomagnetic storm triggered by a CME on 12 July directed toward the Earth (Hess & Zhang, 2014). We consider data sets that include measurements collected a few days prior to and after the storm to properly study the ionospheric response. Figure 3 shows the evolution of geomagnetic

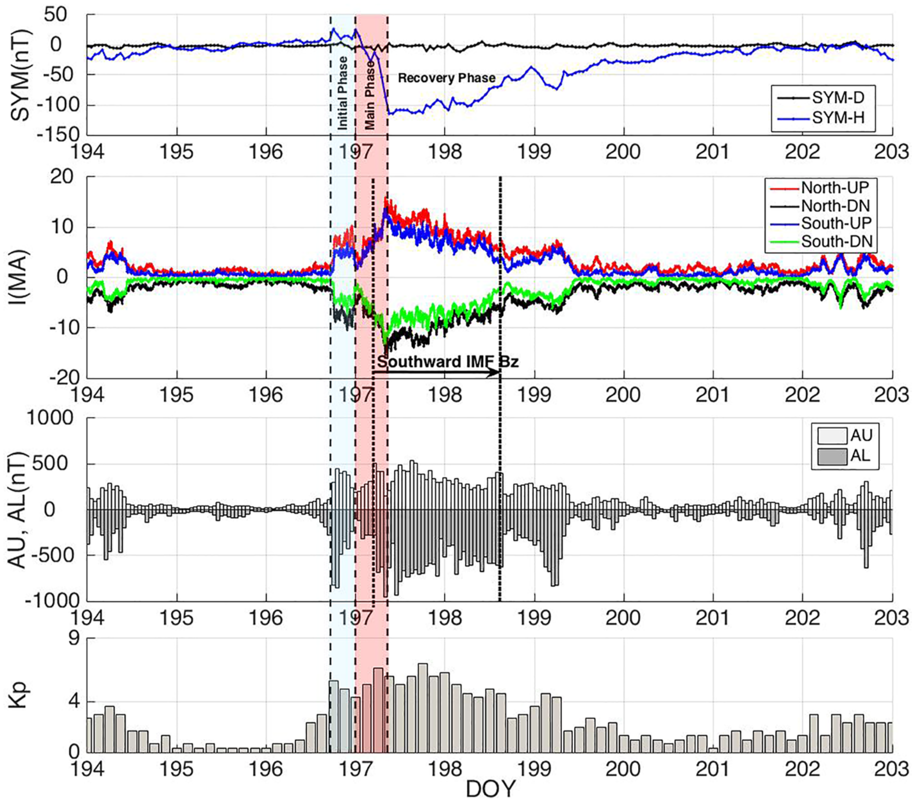

Figure 3. Temporal evolution of selected geophysical parameters for the 14–15 July (DOY: 194–203), 2012, storm. Data from a few days prior to and after the onset of storms are shown. The starts of the initial, main, and recovery phases are marked by vertical dashed lines (light blue and light pink refer to the initial and main phases, respectively). The first panel shows changes in SYM-H/D components. The second panel shows the AMPERE measurements of daytime upward and downward integrated Field-Aligned Currents (FACs) for greater than 60° in the Northern and Southern Hemispheres. The third panel shows the auroral electrojet AU/AL indices, and the fourth panel shows the Kp index. The time window in which IMF B_z turned southward is marked by two vertical dotted lines.

disturbance during 12–21 July (Day of Year; DOY: 194–203). The first panel contains geomagnetic indices attributed to parallel and perpendicular components of the longitudinally symmetric ring current. The index due to the current component parallel to the dipole axis is marked by SYM-H (blue), and this component is generally viewed as a high-resolution version of the Dst index. The index due to the current component perpendicular to the dipole axis is marked by SYM-D (black). The second panel shows AMPERE-observed upward and downward integrated FACs (I) for magnetic latitudes poleward of 60° during the daytime in the Northern and Southern Hemispheres. The third panel in this figure shows the auroral electrojet indices AU and AL, and the fourth panel shows the Kp index. The AU and AL indices refer to upper and lower envelopes of horizontal current perturbations observed along the auroral zone in the Northern Hemisphere (Allen & Kroehl, 1975). The AU index is a measure of the eastward auroral electrojet, flowing in the dayside auroral oval and coupled to magnetopause currents, and AL is a measure of the westward auroral electrojet (e.g., Rostoker, 1996); thus, these parameters indicate a response of the magnetosphere to the changes in the solar wind conditions. The AU/AL indices roughly represent the auroral energy inputs, and the Kp index describes geomagnetic conditions at middle latitudes.

For this storm, SSC occurred at 18:09 UT on 14 July (DOY 196). The three dashed lines in Figure 3 indicate the onsets of the initial, main, and recovery phases. The initial and main phases are shaded with light blue and light pink, respectively. A closer inspection of solar wind parameters at ACE satellite measurements (from NASA-Goddard OMNI data; http://omniweb.gsfc.nasa.gov) indicates that the interplanetary magnetic field (IMF) B_z and B_y components were close to zero on the day before the storm. The solar wind pressure and speed were also small and stable. Shock-like changes in the solar wind parameters occurred ~40 min prior to SSC with a high-level solar wind speed ~600 km/s (Liu et al., 2014). In this figure, sudden increases in FACs in both hemispheres along with abrupt changes in AU/AL and Kp indices occur when SSC occurred. The abrupt changes in the FACs, AU and AL indices, and Kp index indicate high-latitude energy depositions into the polar ionosphere and the formation of convection patterns. Numerous observational and simulation studies provide evidence for these types of dynamic processes at high latitudes due to nonsymmetric ring currents (e.g., Ridley & Liemohn, 2002; Zhang et al., 2007). As a result, SED patches are formed in the polar region during the main phase of the storm (e.g., Foster, 1993; Wang et al., 2019). In our study, this result is also evident in GNSS-RO N_e measurements, as we will briefly discuss below.

During the onset of the storm, the FACs become very dynamic and evolve in accordance with the intensity of reconnection at the daytime magnetopause. As shown in this figure, when the storm proceeds into its main phase on 15 July, SYM-H starts to decrease, and FACs increase in both hemispheres. FACs transfer disturbances of solar origin to auroral latitudes in addition to other forms of energy transfer: high energetic particles and electric fields. Subsequently, the currents reach their maxima ∼12 MA when SYM-H reaches its lowest value, −139 nT. The amplitudes of upward and downward currents in the Northern Hemisphere (red and black) are larger than those in the Southern Hemisphere (blue and green), indicating that relatively more FACs flow in the north. One of the significant features of this storm is the long-lasting southward IMF B_z component during the main phase and recovery phase. Since the occurrence of SSC, the IMF B_z component flips back and forth between north and south, corresponding to the sheath region of the CME-driven shock. During the main phase, the solar wind dynamic pressure increased to ∼28 nPa as a short-lived pulse and decreased to a low value at ∼06:40 UT on 15 July. At this time, the IMF B_z component turned southward and remained southward until ∼15:00 UT on 16 July, while the storm progressed into the recovery phase. The extended southward period corresponds to the ICME flux rope, whose axial field points south (Gopalswamy et al., 2018; Hess & Zhang, 2014). This time window is identified in Figure 3 by two vertical dotted lines in panels 2 and 3. During this interval, very high values of the AL index approaching ∼−1,000 nT, as well as a high Kp index, are recorded, indicating energy inputs into the ionosphere. As the storm progresses into the recovery phase, FACs begin to decrease and reach a low value when IMF B_z turns to the north.

Figure 4 shows a time series of uplooking daytime VTECs from space-based and ground-based observations along with SYM-H and FAC differences between the two hemispheres during 12–21 July (DOY: 194–203). The first and second panels show daytime 3-hr zonal averaged VTEC measurements from COSMIC-1 and GRACE, respectively. The third panel shows the daytime hourly zonal averaged observed VTECs in the ground-based worldwide GNSS receiver system. The fourth panel shows the temporal evolution of the SYM-H index. The fifth panel shows the integrated daytime FAC difference between the two hemispheres ($I_N - I_S$) in the upward (red) and downward (blue) directions. The onsets of the initial, main, and recovery phases are marked by three dashed lines. By orbiting at ∼800-km altitude, COSMIC-1 primarily captures the TEC changes in the plasmasphere from 60°N to 60°S magnetic latitudes (first panel), whereas GRACE, which orbits at ∼450-km altitude, captures both the plasmasphere and topside ionosphere within 80°N and 80°S magnetic latitudes (second panel). As described in Section 2.1, since the orbital time of these satellites is ∼90 min, the contour plots for these two satellites are established using longitudinal means of two successive orbital VTEC measurements. Although this produces repeatable daily artifacts (as noticeable in Figure 4 prior to the storm), the temporal evolution of VTECs during the storm shows good agreement among COSMIC-1, GRACE, and ground-based observations. At the onset of the initial phase (first dashed line), dramatic changes in the VTECs are evident at midlatitude and high latitude in the Northern Hemisphere. When the storm progresses into the main phase, all data products show a substantial increase in VTECs extending across wider latitudes. COSMIC-1 VTEC (above ∼800 km) and GRACE VTEC (above ∼450 km) observations represent ∼20% and ∼80% of the ground-based observations, consistent with previous daytime studies (Belehaki et al., 2004; Cherniak et al., 2012; Yizengaw et al., 2008). As shown in Figure 3, the FACs, AU/AL indices, and Kp index continuously increase during this phase, and in particular, the FACs reach a maximum at the end of the main phase (see Figure 4 bottom panel).

In the GNSS-RO N_e measurements from COSMIC-1 and GRACE, they provide a 3D latitude, time, and altitude view for the storm-induced N_e changes. Figure 5 shows a horizontal view of the retrieved daytime N_e at 240-km, 280-km, and 300-km altitudes during 12–21 July (DOY: 194–203). The daytime GNSS-RO N_e measurements from both satellites are combined and zonally averaged to 6 hr, as described in Section 2.1. During the onset of the storm, in addition to increases in N_e in the equatorial and low-latitude regions, the figure also shows the occurrence of increases in N_e at ∼60°N, especially during the initial and early main phases. Respective height-time

10.1029/2021JA030247

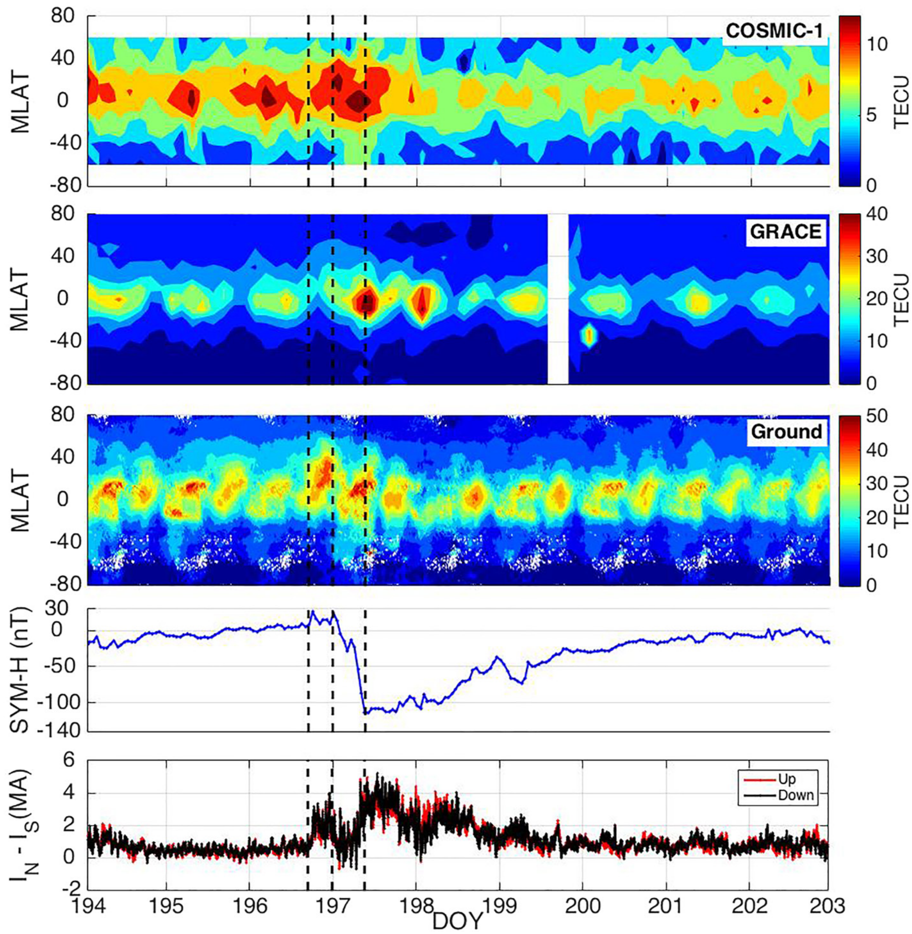

Figure 4. Time series of uplooking daytime vertical TEC (VTEC) observations from COSMIC-1 (first panel), GRACE (second panel), and ground-based (third panel) within 80°N and 80°S magnetic latitudes during 12–21 July (DOY: 194–203). The temporal evolution of the SYM-H index is shown in the fourth panel. The difference in integrated daytime Field-Aligned Currents (FACs) between the Northern and Southern Hemispheres ($I_N - I_S$) is shown in the fifth panel. Red refers to an upward FAC difference, and black refers to a downward FAC difference.

curtain views across 60°N and 60°S magnetic latitudes are shown in Figure 6. At 60°N (first panel), the increase in N_e starts to occur during the initial hours of the storm at ~300 km. Subsequently, during the early main phase, this increase in N_e is uplifted and then decreases below the prestorm value once the recovery phase starts. Since the magnetic fields are not strictly vertical in this region, this uplifting of plasma to higher altitudes is anticipated during plasma convection, as reported in previous studies (e.g., Heelis et al., 2009; Zou et al., 2014, and several others). On the other hand, in the case of 60°S (second panel), this type of large-scale enhancement and uplifting of N_e starts occurring toward the end of the main phase. The observed time delay between 60°N and 60°S appears to be in good agreement with the observed TEC, especially with ground-based observations (panel 3 in Figure 4).

Returning to Figure 4, when the storm transitions from the main phase to the recovery phase, a substantial amount of depletions in the VTECs are visible in all three data products. Depletions start to appear initially at northern high latitudes and then progress into midlatitude and low latitude. During the recovery phase, the VTECs in midlatitude and low latitude are reduced by ~25% in COSMIC-1 observations and ~17% in GRACE observations. At the same time, the FACs remain high and active for more than ~48 hr during the recovery phase. The panels also indicate a slow recovery of the ionosphere and plasmasphere until SYM-H returns closer to zero by DOY 201.

In the case of the AMPERE measurements of FACs during this storm, the integrated FACs in the north are higher than those in the south, as is evident in panel 5 in Figure 4. The difference between I_N and I_S starts to occur during

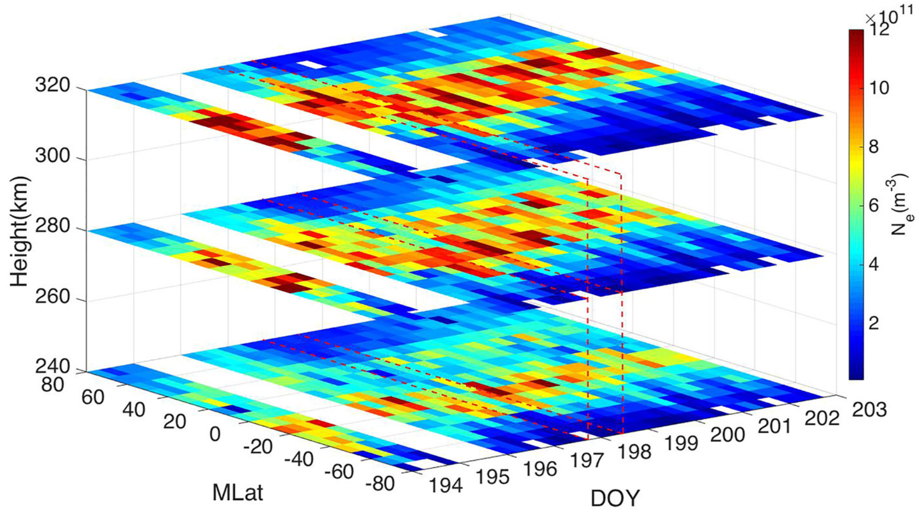

Figure 5. Horizontal view of measured daytime GNSS-RO N_e at 240-km, 280-km, and 300-km altitudes during 12–21 July (DOY: 194–203). The onset of the initial phase and the end of the main phase are marked by dashed lines. The curtain views for N_e at 60°N and 60°S are shown in Figure 6.

the initial phase, and consequently, the difference reaches higher than 4 MA at the end of the main phase. This difference remains high for several hours into the recovery phase. In this figure, the high integrated FAC flow in the north compared to the south (i.e., $I_N - I_S > 0$) shows a good agreement with VTEC depletions in the northern hemisphere that is especially prominent in the cases of GRACE and ground-based data. The solstice in the Northern Hemisphere occurred 24 days preceding this storm; thus, the ionization rate is higher in the north than in the south due to a greater amount of sunlight. Hence, the high ionospheric conductivity in the northern summer might have played a role in increasing northern FACs compared to the southern FACs when the storm has struck. This change might, in turn, increase the ionospheric heating process, leading to faster phase composition changes

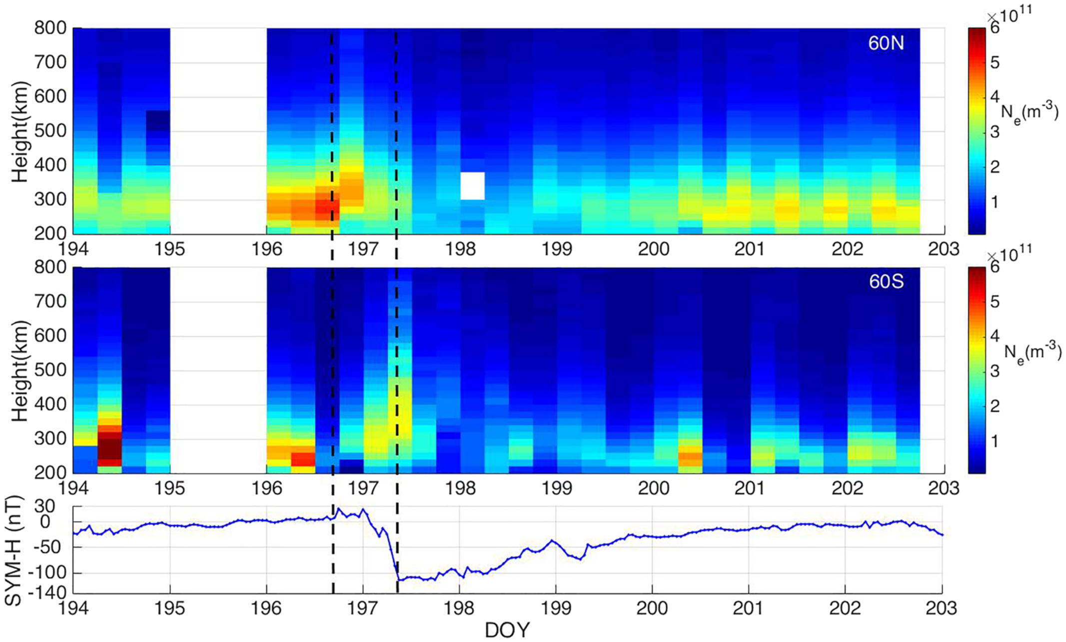

Figure 6. Comparison of measured daytime GNSS-RO N_e height-time curtain views across 60°N and 60°S magnetic latitudes during 12–21 July (DOY: 194–203). At 60°N, large-scale enhancement of N_e starts to occur at ~300 km and higher altitudes during the initial hours of the storm (first panel), whereas at 60°S, a similar feature occurs toward the end of the main phase (second panel). The onset of the initial phase and the end of the main phase are marked by dashed lines.

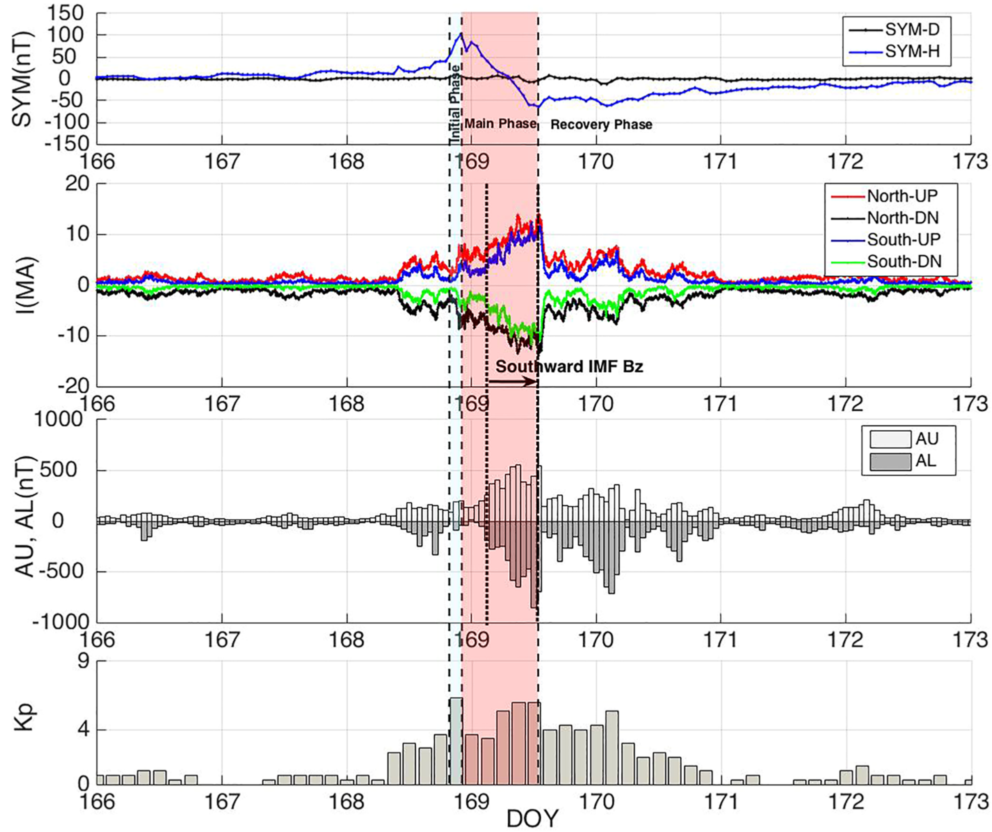

Figure 7. Temporal evolution of selected geophysical parameters during 14–21 June 2012 (DOY: 166–173). Data from a few days prior to and after the storm are shown. The onsets of the initial, main, and recovery phases are marked by vertical dashed lines (light blue and light pink refer to the initial and main phases, respectively). The first panel shows changes in SYM-H/D components. The second panel shows the AMPERE measurements of daytime upward and downward integrated Field-Aligned Currents (FACs) for greater than 60° in the Northern and Southern Hemispheres. The third panel shows the auroral electrojet AU/AL indices, and the fourth panel shows the Kp index. The time window in which IMF B_z turned southward is marked by two vertical dotted lines.

in the north relative to the south. Although the hemispheric asymmetry in ionospheric responses is generally explained as a result of composition changes carried away by perturbed equatorward meridional winds (e.g., Prölss, 1997), the concept is still actively debated, and we will return to the discussion of this topic after describing other geomagnetic storms.

3.2. 16–17 June 2012 Storm

The 16–17 June 2012 event was a moderate geomagnetic storm. The ionospheric response for this storm is very similar to that of the July 2012 storm. The storm was triggered by two successive CMEs within 25 hr directed toward the Earth on 13 and 14 June, respectively (OMNI data; http://omniweb.gsfc.nasa.gov). The second CME had a higher speed than the first CME, and the two CMEs interacted on their path to the Earth and reached the Earth as a merged structure (Srivastava et al., 2018). At ACE, the first shock arrived at 08:42 UT on 16 June with a speed of ~450 km s^{-1}, and the second shock arrived on the same day at 21:40 UT with a speed of ~485 km s^{-1}. Figure 7 shows the evolution of geomagnetic disturbance during 14–21 June (DOY: 166–173). The first panel shows the geomagnetic SYM-H and SYM-D indices. The SYM-H index rose from 39 to 150 nT before it started to plunge to −86 nT. An increase in the SYM-H amplitude by >100 nT is extremely rare (<1%) during SSCs (e.g., Maeda et al., 1962; Srivastava et al., 2018). The second panel shows upward and downward integrated daytime FACs for magnetic latitudes poleward of 60° in the Northern and Southern Hemispheres, as determined by the AMPERE. The third panel shows the auroral electrojet indices AU and AL, and the fourth panel shows the Kp index. When the first SSC occurred, the IMF B_y component was negative, and B_z started to fluctuate between

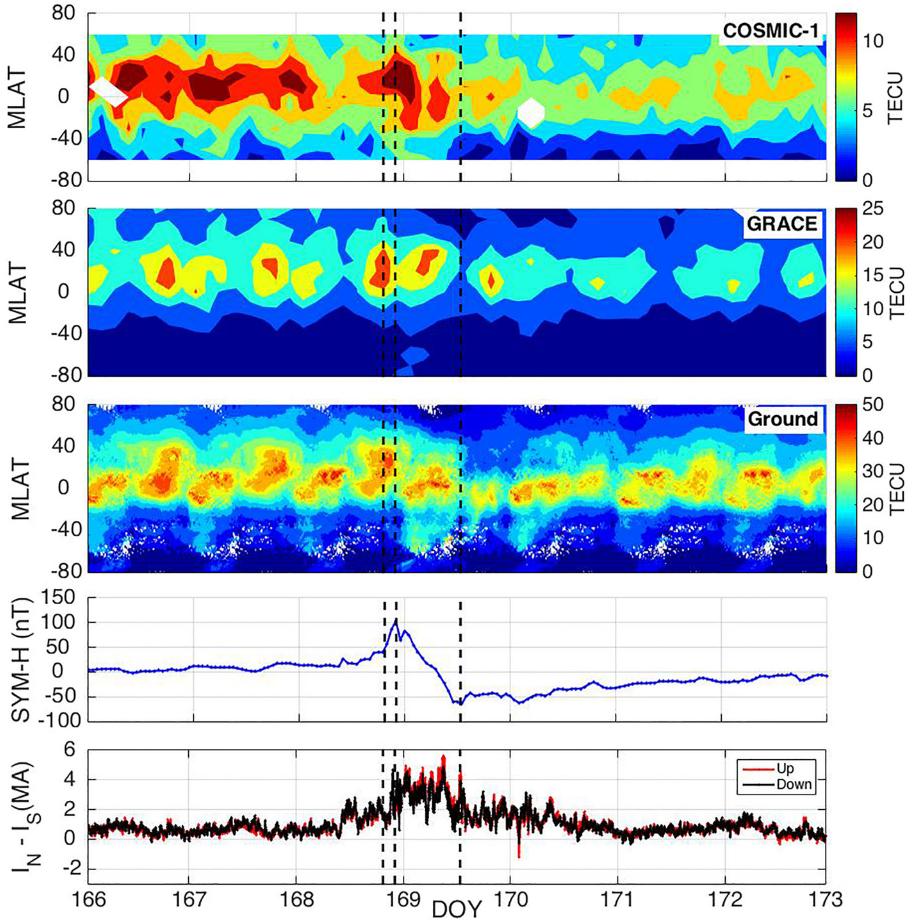

Figure 8. Time series of uplooking daytime vertical TEC (VTEC) observations from COSMIC-1 (first panel), GRACE (second panel), and ground-based (third panel) receivers within 80°N and 80°S magnetic latitudes during 14–21 June 2012 (DOY: 166–173). The temporal evolution of the SYM-H index and integrated daytime Field-Aligned Current (FAC) difference between the Northern and Southern Hemispheres ($I_N - I_S$) are shown in the fourth and fifth panels, respectively.

positive and negative until the second SSC occurred. After the second SSC, B_z remained positive for ∼2 hr before becoming negative at ∼4:00 UT on 17 June. Similar to the previous storm, FACs start to increase in both hemispheres when SSC occurs; in particular, they increase steadily up to the end of the main phase. In addition, the AU and AL indices (third panel) increased, which is an indication of high-latitude energy deposition into the polar ionosphere and the formation of convection patterns.

Figure 8 shows a time series of the uplooking daytime VTECs from COSMIC-1 (first panel), GRACE (second panel), and ground-based GNSS receivers (third panel) within 80°N and 80°S magnetic latitudes during 14–21 June (DOY: 166–173). Note that COSMIC-1 VTEC coverage is shown from 60°N to 60°S magnetic latitudes. The space-based observations are daytime 3-hr zonal averaged, and the ground-based observations are daytime hourly zonal averaged. The fourth panel shows the SYM-H index, and the fifth panel contains the integrated daytime FAC difference ($I_N - I_S$) between the two hemispheres in the upward (red) and downward (blue) directions. The onsets of the initial, main, and recovery phases are marked by three dashed lines. Figure 8 shows that the temporal evolutions of VTECs among COSMIC-1, GRACE, and ground-based observations are in good agreement during the entire period of 14–21 June.

Similar to Figure 6, the time delay associated with daytime large-scale N_e enhancements and uplifting between the summer and winter high latitudes is also evident in this storm when comparing the curtain views across 60°N and 60°S in the GNSS-RO N_e observations. In this case, in the northern high latitudes, large-scale enhancements and uplifting occur during the initial and early main phases, and similar features occur in the southern high latitudes during the late main phase (figure not shown). As detected in the July storm, the observed feature in

10.1029/2021JA030247

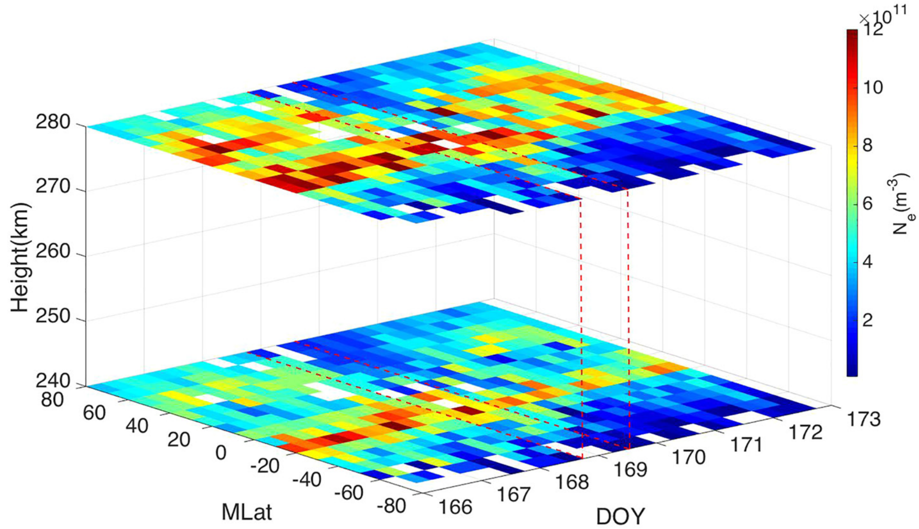

Figure 9. Horizontal view of measured daytime GNSS-RO N_e at 240-km and 280-km altitudes during 14–21 June 2012 (DOY: 166–173). The onset of the initial phase and the end of the main phase are marked by dashed lines.

N_e appears to be consistent with the TEC observations, especially in the ground-based observation (panel 3 in Figure 8). Subsequently, depletions start to occur at high latitudes and progress to midlatitude and low latitude. In addition, differences in the AMPERE integrated FACs between the north and south ($I_N - I_S$) are also very similar to those in the July storm. However, significant changes in $I_N - I_S$ (exceeding 4 MA) start to appear during the main phase in this storm, whereas in the July storm, it occurs once the recovery phase started. Furthermore, in the ground-based VTEC observation, several hours of VTEC depletion to as low as 20°N in the Northern Hemisphere are also noticed (panel 3 in Figure 8). In addition, strong N_e depletions at F-region altitudes are evident in the GNSS-RO N_e measurements. Figure 9 captures the horizontal structure of N_e, combined from the two satellites listed above at 240-km and 280-km altitudes during 14–21 June (DOY: 166–173). While a strong level of electron density depletion occurs in the northern high latitudes during the early phases of the storm, these changes are not prominent in the Southern Hemisphere until the storm reaches the recovery phase. Notably, this storm occurred only 3 days preceding the summer solstice in the Northern Hemisphere, and the analysis of dayside VTEC and GNSS-RO N_e along with the AMPERE FACs indicates that preconditioning in the Northern Hemisphere might have played a significant role in triggering interhemispheric asymmetry in the response of the ionosphere.

3.3. 19–20 December 2015 Storm

The 19–20 December 2015 event was an intense geomagnetic storm in which the SYM-H index reached the minimal value of −170 nT. Unlike the previous two storms, this storm occurred during summer in the Southern Hemisphere. As in the June 2012 storm, this storm also occurred as a consequence of two successive CMEs. The shock arrived at ACE at ∼15:40 UT on 19 December, and the second but slower CME also propagated within interplanetary space (Gopalswamy, Yashiro et al., 2015). However, since the second CME was not from the same region of the Sun, the possible interaction between the two CMEs was unlikely. Before the onset of the storm, solar wind remained at a speed of ∼350 km s^{-1}. When SSC occurred at ∼16:20 UT, the speed increased to ∼475 km s^{-1}. During the initial phase of the storm, IMF B_z started to fluctuate between positive and negative but remained mostly positive until the early hours of 20 December. Figure 10 shows the evolution of geomagnetic parameters during 18–27 December (DOY: 352–361). The first panel shows the geomagnetic SYM-H and SYM-D indices of the longitudinally symmetric ring current, and the SYM-H index reaches −155 nT at the end of the main phase. The second panel shows upward and downward integrated daytime FACs for magnetic latitudes poleward of 60° in the Northern and Southern Hemispheres, as determined by the AMPERE. The third panel shows the auroral electrojet indices AU and AL, and the fourth panel shows the Kp index. When B_z turns southward, FACs start to increase to higher than 10 MA in both hemispheres, as observed in the other two geomagnetic storms. Note that the amplitude of the integrated upward and downward currents (blue and green) for the Southern Hemisphere is

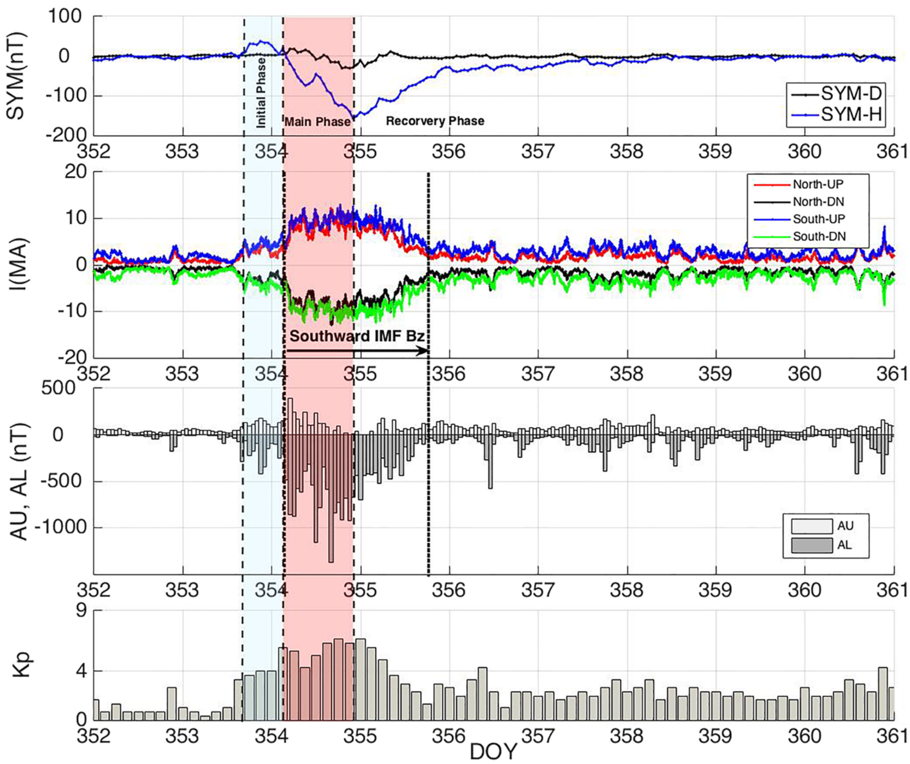

Figure 10. Temporal evolution of selected geophysical parameters during 18–27 December 2015 (DOY: 352–361). Data from a few days prior to and after the storm are shown. The onsets of the initial, main, and recovery phases are marked by vertical dashed lines (light blue and light pink indicate the initial and main phases, respectively). The first panel shows changes in SYM-H/D components. The second panel shows the AMPERE measurements of daytime upward and downward integrated Field-Aligned Currents (FACs) for greater than 60° in the Northern and Southern Hemispheres. The third panel shows the auroral electrojet AU/AL indices, and the fourth panel shows the Kp index. The time window in which IMF B_z turned southward is marked by two vertical dotted lines.

larger than the amplitude in the Northern Hemisphere (red and black) compared to the cases in the previous two storms, which occurred during summer in the Northern Hemisphere. Meanwhile, the AL index increases sharply to greater than 1,000 nT along with the Kp index to the maximum value of 7. As is evident in this figure, the temporal evolution of these geomagnetic parameters is very similar to that of the two previous storms. Nevertheless, VTEC and GNSS-RO electron density observations indicate a different picture in the December 2015 storm compared to the other two storms.

Figure 11 shows the time series of the uplooking daytime VTECs from MetOp-A/B (first panel), GRACE (second panel), and ground-based GNSS receivers (third panel) within 80°N and 80°S magnetic latitudes during 18–27 December. The fourth panel shows the SYM-H index, and the fifth panel presents the integrated daytime FAC difference ($I_N - I_S$) between the two hemispheres in the upward (red) and downward (blue) directions. For this storm, since the number of PODTEC samples in COSMIC-1 is fewer than that in MetOp-A/B, especially during December 2015, we decided to use MetOp-A/B, which has coverage from 70°N to 70°S magnetic latitudes. The orbital altitude of MetOp-A/B is ~830 km, which is only 30 km higher than COSMIC-1; hence, incorporating MetOp-A/B will not affect our topside ionospheric VTEC analysis and comparisons. The onsets of the initial, main, and recovery phases of this storm are marked by three dashed lines. In this figure, the recovery time for this storm is relatively short compared to the previous two storms. More importantly, the increases in VTECs start to occur in the Southern Hemisphere in MatOp-A/B, GRACE, and ground-based observations, particularly during the main phase. Subsequently, depletions occur in all three data products in the Southern Hemisphere. Additionally, as shown in panel 5, the FACs in the Southern Hemisphere are higher than the FACs in the Northern Hemisphere during the onset of this storm. However, the mean increase in the integrated FACs in the Southern Hemisphere is slightly lower (~3 MA) than the means of the previous two cases (~4 MA). Compared to the other two storms, the negative values of $I_N - I_S$ during the onset of this storm indicate that preexisting summer

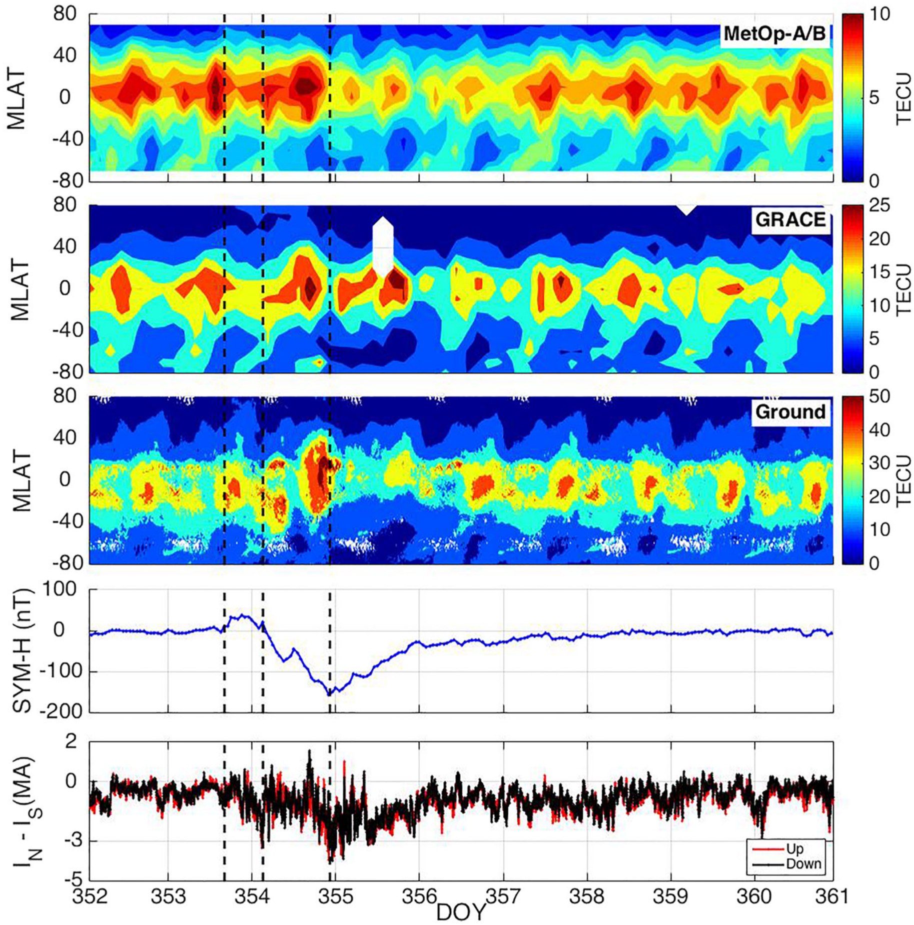

Figure 11. Time series of the uplooking daytime vertical TEC (VTEC) observations from MetOp-A/B (first panel), GRACE (second panel), and ground-based (third panel) receivers within 80°N and 80°S magnetic latitudes during 18–27 December 2015 (DOY: 352–361). The temporal evolution of the SYM-H index and integrated daytime Field-Aligned Current (FAC) difference between the Northern and Southern Hemispheres ($I_N - I_S$) is shown in the fourth and fifth panels, respectively.

ionospheric conditions in the Southern Hemisphere possibly affect the N_e responses and hence the hemispheric asymmetry in the VTECs.

In the preceding sections, we have described and discussed the results of three geomagnetic storms from space-based and ground-based observations. The first two storms occurred during summer in the Northern Hemisphere. The first storm occurred 24 days after the summer solstice, and the second storm occurred 3 days prior to the summer solstice. On the other hand, the third geomagnetic storm occurred a day prior to the summer solstice in the Southern Hemisphere. The observed upward-looking VTECs from multiple LEO satellites at different orbital altitudes (~450 and 800 km), as well as from the ground-based GNSS network, show good agreement with the ionospheric response for these storms. These results indicate that summer preconditioning influences the ionospheric daytime response to these geomagnetic storms. Hence, a question arises as to how the ionosphere responds if storm onset occurs on days closer to or on the day of the equinox. We considered a storm that occurred at St. Patrick's Day in 2015 to answer this question.

3.4. 17–18 March 2015 Storm

A super geomagnetic storm occurred on 17–18 March 2015 with the SYM-H index reaching the minimal value of −223 nT. This storm was termed the St. Patrick's Day storm and the most intense magnetic storm in solar cycle 24. Several studies on this storm from different perspectives have been published (Astafyeva et al., 2015; Wu et al., 2016; Zhang et al., 2017, and references therein). The storm was caused by an Earth-directed CME, which

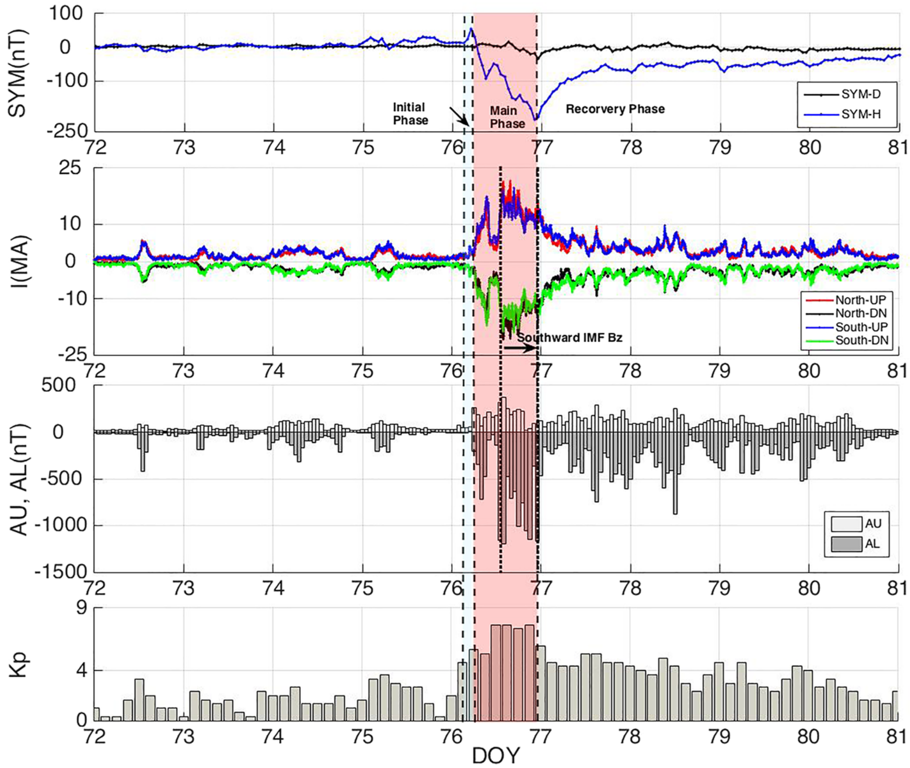

Figure 12. Temporal evolution of selected geophysical parameters during 13–22 March 2015 (DOY: 072–081). Data from a few days prior to and after the storm are shown. The onsets of the initial, main, and recovery phases are marked by vertical dashed lines (light blue and light pink indicate the initial and main phases, respectively). The first panel shows changes in SYM-H/D components. The second panel shows the AMPERE measurements of daytime upward and downward integrated Field-Aligned Currents (FACs) for greater than 60° in the Northern and Southern Hemispheres. The third panel shows the auroral electrojet AU/AL indices, and the fourth panel shows the Kp index. The time window in which IMF B_z turns southward is marked by two vertical dotted lines.

erupted on 15 March 2015 (e.g., Gopalswamy, Tsurutani et al., 2015). SSC was registered at ∼04:45 UT on 17 March with an increase in the solar wind speed from 400 km s^{-1} to higher than 500 km s^{-1} and the dynamic pressure increased by 20 nPa. During the initial phase of the storm and a few hours in the early part of the main phase, IMF B_z oscillated between the north and the south and turned southward at ∼13:40 UT until the end of the day.

Figure 12 shows the evolution of geomagnetic parameters during 13–22 March. The first panel shows the geomagnetic SYM-H and SYM-D indices, and the SYM-H index reaches −223 nT at the end of the main phase. The integrated daytime FACs from AMPERE, which are shown in the second panel, start to increase, reaching a maximum of ∼12 MA in both the upward and downward directions, and then start to decrease. During this interval, the AL index sharply increases, reaching a maximum higher than 1,000 nT at the end of the main phase (third panel). Moreover, the Kp index reaches its maximum of ∼8 during this interval (fourth panel). Figure 13 shows a time series of the uplooking daytime VTECs from MetOp-A/B (first panel), GRACE (second panel), and ground-based GNSS receivers (third panel) within 80°N and 80°S magnetic latitudes during 13–22 March. The variations in VTECs between the two LEO satellites and the ground-based GNSS network show good agreement. The increases in VTECs during the main phase appear relatively symmetric compared with previous storms. Moreover, subsequent depletions during the recovery phase also symmetrically occur in the Northern and Southern Hemispheres. Additionally, the FAC difference ($I_N - I_S$) continues to exhibit negative values in the early hours of the main phase with a spike of −5 MA and becomes positive with a maximum of 4 MA. Unlike in the previous storms, the quantity $I_N - I_S$ appears to fluctuate back and forth between positive and negative during this storm. The storm occurred only 3 days prior to the vernal equinox. Similar to the December 2015 storm, this storm also quickly recovered almost within a day. Nevertheless, MetOp-A/B VTEC indicates that the recovery time window

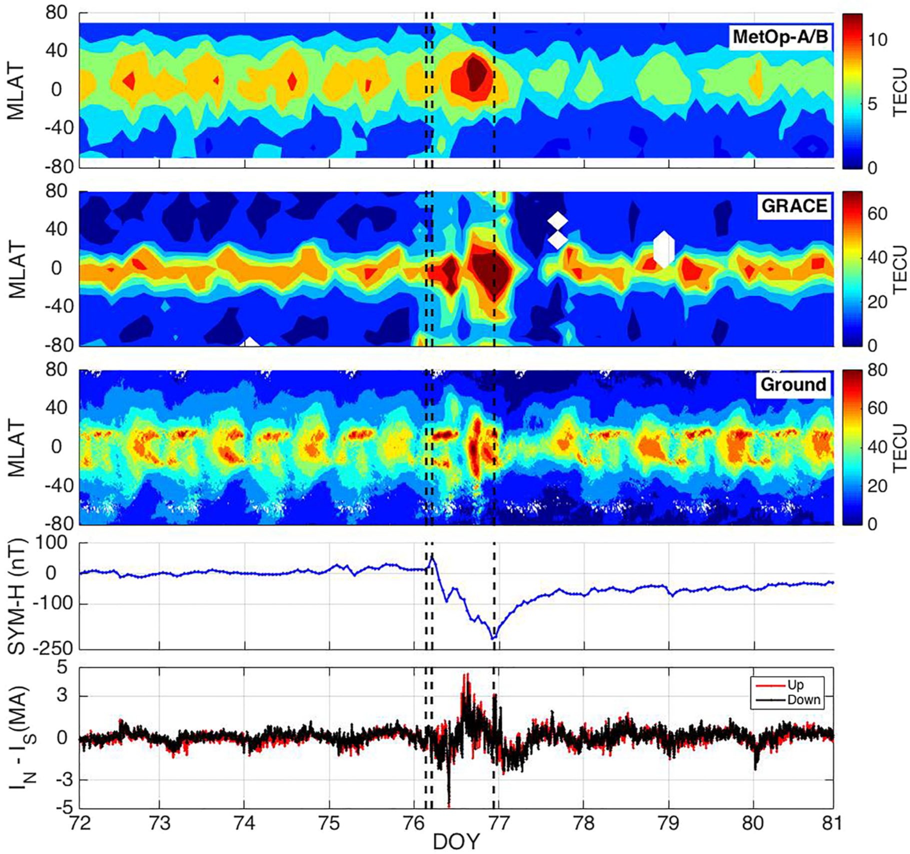

Figure 13. Time series of the uplooking daytime vertical TEC (VTEC) observations from MetOp-A/B (first panel), GRACE (second panel), and ground-based (third panel) receivers within 80°N and 80°S magnetic latitudes during 13–22 March 2015 (DOY: 072–081). The temporal evolution of the SYM-H index and integrated daytime Field-Aligned Current (FAC) difference between the Northern and Southern Hemispheres ($I_N - I_S$) are shown in the fourth and fifth panels, respectively.

is relatively high compared to GRACE and ground observations. Notably, the MetOp orbital altitude is ∼830 km; hence, this receiver might indicate a slow recovery in the plasmasphere compared to the ionosphere.

4. Daytime and Nighttime TEC Perturbations

In the previous section, interhemispheric asymmetry is evident in daytime VTEC depletions during geomagnetic storms, which occurred in June 2012, July 2012, and December 2015. During the onset of the June and July storms, depletions prominently occur in the northern high latitude and midlatitude, whereas during the onset of the December storm, the depletions occur in the Southern Hemisphere. On the other hand, the interhemispheric N_e response during the March 2015 storm is relatively symmetric compared with previous cases. VTEC observations from all three data products show good agreement in all of the aforementioned storms. In addition, GNSS-RO N_e from COSMIC-1 and GRACE also show good agreement with the observed feature described above. At the same time, at high latitudes greater than 60°, the integrated FACs from AMPERE are relatively high in the Northern Hemisphere for the June 2012 and July 2012 storms and low for the December 2015 storm, suggesting that more FACs flow in the summer hemisphere during the onset of these storms compared to the winter hemisphere. This hemispheric asymmetrical pattern is not evident either in TEC observations or AMPERE FACs during the March 2015 storm.

As described in Section 2, low global sampling rates produce artifacts in both space-based and ground-based data sets. However, as noticed in the previous TEC figures (Figures 4, 8, 11, and 13), these artifacts are repeatable on a daily basis and can be removed using quiet-time TECs. In this section, we remove these artifacts and investigate daytime and nighttime perturbations in VTECs separately during storms. For this purpose, we consider ∼10 quiet

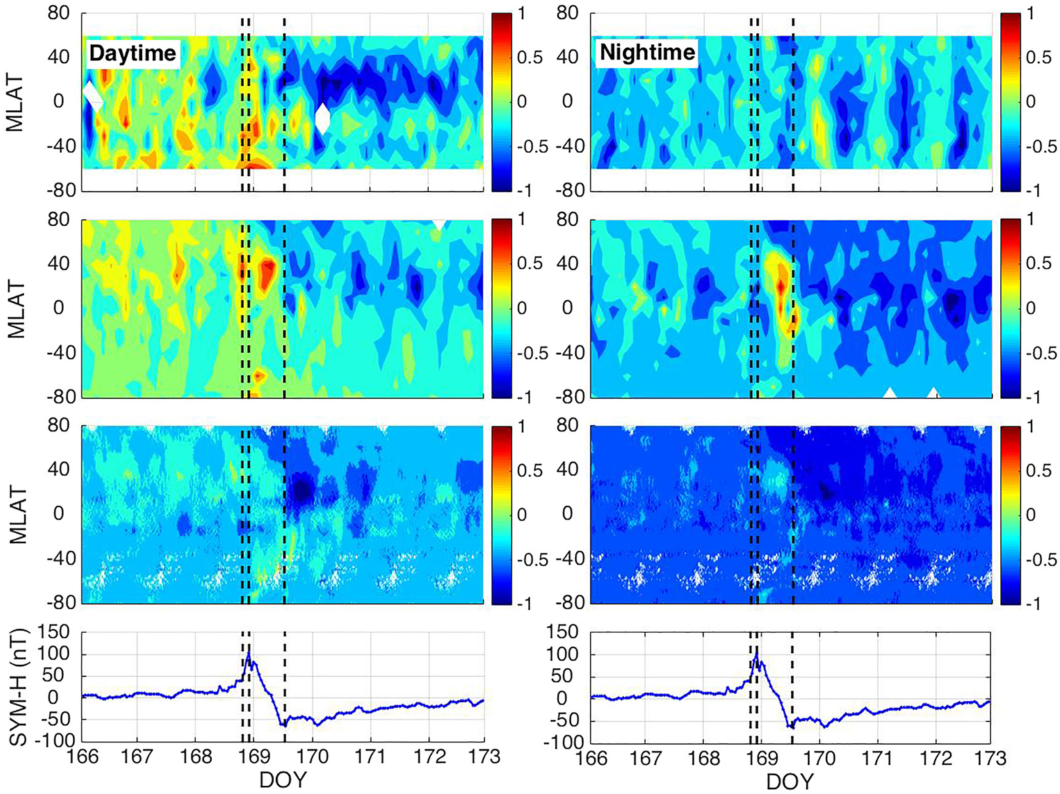

Figure 14. Time series of the estimated perturbation in vertical TEC (VTEC) for daytime (left panel) and nighttime (right panel) during the June 2012 geomagnetic storm. The first panel shows COSMIC-1 for daytime and MetOp-A for nighttime. The second and third panels show the perturbations in GRACE and ground-based measurements, respectively. The time series are normalized from peak to peak.

days before and after storms (with a Dst index higher than −50 nT and Kp < 4) and estimate the mean diurnal VTEC variation for quiet days. Subsequently, we subtract the quiet-day absolute VTECs from the storm-day VTECs (e.g., Immel & Mannucci, 2013). Since the VTEC differences, Δ(VTEC), vary widely from one data product to another, we normalize them using the respective quiet-day absolute VTEC and set the lowest value of the ratio to −1 and highest to +1. This approach will facilitate an easy comparison among different data products and better capture the small spatiotemporal changes in VTECs (e.g., Shinbori et al., 2020).

The removal of background VTECs during storms makes the hemispheric asymmetrical feature more pronounced. Figure 14 shows the normalized perturbation time series for the geomagnetic storm that occurred in June 2012. The left column shows perturbations during daytime, and the right column shows the same for nighttime. The first panel shows VTEC perturbations in COSMIC-1 (daytime) and MetOp-A (nighttime) observations. The second and third panels show the perturbations in GRACE and ground-based observations, respectively. The onsets of the initial, main, and recovery phases are marked by vertical dashed lines. In the main phase, the daytime VTEC depletions start initially at northern high latitudes and progress to midlatitude and low latitude when the storm transitions to the recovery phase. This change is evident in all three data products. In the case of nighttime observations, the VTEC depletion patterns are very similar to those recorded in the daytime, at least in GRACE and ground-based observations. This result may indicate the level of the effect of the daytime VTEC changes on the nighttime ionosphere. In this figure, the nighttime VTEC perturbations extend to wider latitudes. In the case of the July 2012 storm (not shown), the VTEC perturbations are very similar to those of the June 2012 storm.

In the case of the December 2015 storm, Figure 15 shows normalized VTEC perturbation time series for MetOp-A/B (first panel), GRACE (second panel), and ground-based (third panel) observations. In this case, the daytime plot (left side) shows that the VTEC depletions start at high latitudes in the Southern Hemisphere and progress into midlatitude and low latitude. These features are opposite to those that have been observed in the June 2012 storm and July 2012 storm. For comparison, we also include VTEC perturbations for the March 2015 storm.

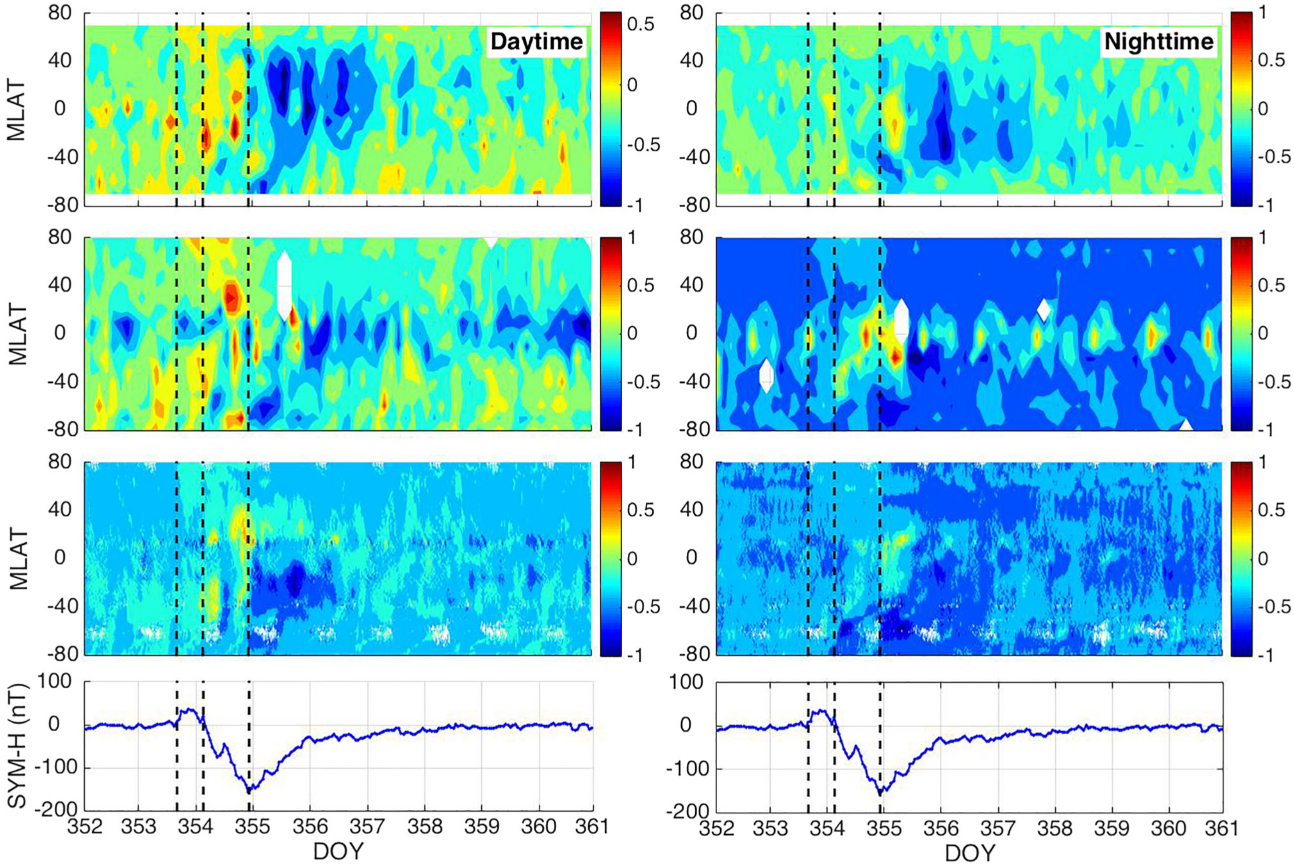

Figure 15. Time series of the estimated perturbations in vertical Total Electron Contents (VTECs) in the daytime (left panel) and nighttime (right panel) during the geomagnetic storm that occurred in December 2015. The first panel shows the estimation from MetOp-A/B measurements. The second and third panels show the same estimations from GRACE and ground-based measurements, respectively. The time series are normalized to peak to peak.

Figure 16 shows the VTEC perturbations for the March 2015 storm in MetOp-A/B (first panel), GRACE (second panel), and ground-based (third panel) observations. As shown in this figure, the perturbation analysis for this storm does not show any interhemispheric asymmetry in any of the data products. The results show a symmetric feature in VTEC depletions.

Using a large number of VTEC and N_e measurements from multiple LEO satellites and ground-based GNSS receivers, we observe interhemispheric asymmetry in ionospheric N_e perturbations in the geomagnetic storms described above. By removing the background daily variation using the quiet-day data, we show that the N_e depletions are pronounced in summer months in both hemispheres during the onset of the recovery phase. Our results also indicate that global-scale depletions initially occur at summer high latitudes during the main phase of the storm and then progress to midlatitude and low latitude when storms move into the recovery phase. The three storms (16–17 June and 14–15 July 2012, and 19–20 December 2015) studied here occurred either a few days prior to or after the summer solstice. However, this pronounced interhemispheric asymmetry is not evident in the March storm. Using a modeling study, Balan et al. (1995) previously showed that interhemispheric plasma flows driven by meridional transequatorial neutral winds from the summer to the winter hemisphere during the daytime lead to stronger TECs and N_e in the equatorial ionization anomaly (EIA), especially in the winter hemispheric low latitude and midlatitude. Later, N_e measurements from CHAMP showed that the most significant changes in low latitude and midlatitude occur during the main phase, and subsequently, the chemical effects produce negative ionospheric storms at all latitudes during the recovery phase (Balan et al., 2011). In our analysis, these signatures are evident during the December 2015 (austral summer) storm in both space-based and ground-based observations. As illustrated in Figure 15, significant increases in daytime TECs occur during the main phase in the winter hemispheric low latitudes, implying strong summer-to-winter plasma flows. On the other hand, in the case of the March 2015 (equinoctial) storm, the EIA appears quite symmetric, implying weak summer-to-winter

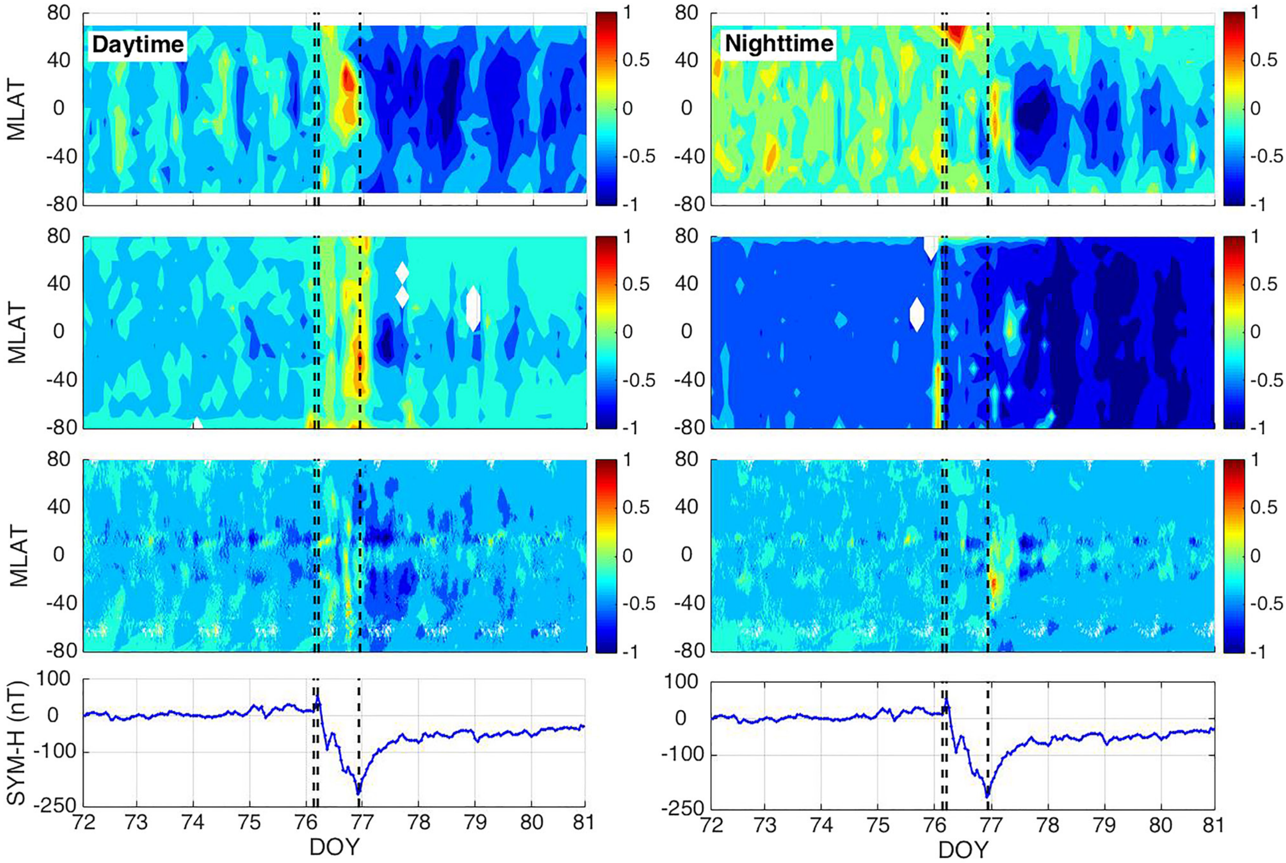

Figure 16. Time series of the estimated perturbations in vertical Total Electron Contents (VTECs) in the daytime (left panel) and nighttime (right panel) during the geomagnetic storm that occurred in March 2015. The first panel shows the estimation from MetOp-A/B measurements. The second and third panels show the same estimations from GRACE and ground-based measurements. The time series are normalized from peak to peak.

plasma flows. However, evidence for these signatures was not clearly observed during the June and July 2012 (boreal summer) storms. This difference might be because sometimes the signatures of summer-to-winter plasma flows are not as clear cut due to the simultaneous actions of different physical mechanisms, as described by Bruinsma et al. (2006).

Although the space-based and ground-based TEC observations are from different altitudinal ranges, the good agreement among them indicates that the global large-scale ionospheric latitudinal storm responses are very similar. However, we are not excluding the existence of regional differences associated with these storms over regional territories. Indeed, previous case studies of the July 2012 storm using ground-based GNSS receivers (Liu et al., 2014) and over oceans along the track of downlooking TEC measurements from the Jason-2 satellite (Kuai et al., 2017) showed regional differences in TEC changes between American and Australian-Asian sectors and a prolonged negative ionospheric phase in the American sector. Similar results were also reported in case studies on the March 2015 storm (e.g., Astafyeva et al., 2015; Polekh et al., 2017). Since our TEC results are based on hourly zonal means in the case of ground-based observations and 3-hr zonal means in the case of ground-based observations, they may not be able to capture regional differences within shorter time scales.

5. Discussion

In the previous section, interhemispheric asymmetry is evident in daytime VTEC and N_e depletions, especially for geomagnetic storms that occurred in boreal and austral summer months. In particular, VTEC observations from GRACE and ground-based GNSS receivers show clear seasonal effects on the latter part of the main phase and recovery phase. Figure 17 shows the integrated daytime FAC differences (i.e., $I_N - I_S$) between the Northern and Southern Hemispheres for all four storms. The red line represents data collected every 2 min, and the black

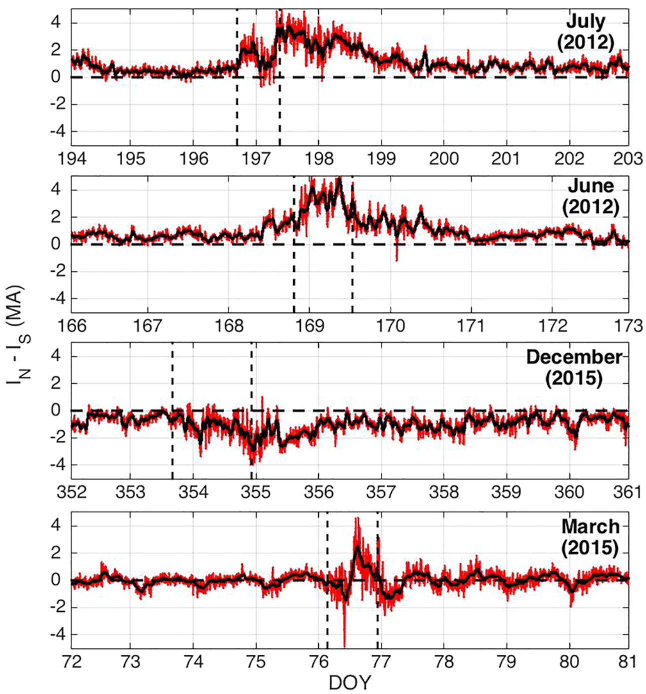

Figure 17. Comparison of Field-Aligned Current (FAC) differences between the Northern and Southern Hemispheres in the daytime during the onset of the four storms. I_N and I_S are integrated FACs for magnetic latitudes poleward of 60° for the Northern and Southern Hemispheres. The red line represents data collected every 2 min, and the black line refers to the 30-min mean. The two vertical dashed lines confine the start of the initial phase and end of the main phase of the storm.

line refers to 30-min mean values. The two vertical dashed lines confine the start of the initial phase and the end of the main phase of the storm. As shown in this figure, $I_N - I_S$ remained positive for the June and July 2012 storms and negative for the December 2015 storm. On the other hand, this hemispheric asymmetrical pattern is not prominent for the storm that occurred in the equinoctial month (March 2015). Earlier, Sugiura and Potemra (1978) reported seasonal dependence in net Birkeland currents. This result was confirmed later by Fujii et al. (1981), and the dayside Birkeland currents are larger during the local summer by a factor of 2 compared to winter. Recent studies using AMPERE indicate that FACs are consistent with magnetic reconnections on the dayside of Earth and that currents are seasonally dependent, peaking in the local summer hemisphere (e.g., Anderson et al., 2014). Moreover, studies also show that more currents flow in northern summer than in southern summer (Coxon et al., 2016). Although these studies were conducted under stationary conditions, our observations on FACs during storm conditions are consistent with previous studies. In Figure 17, the days prior to the onset of the storm exhibit a slightly high FAC flow in the summer hemisphere compared to the winter hemisphere, and this difference in magnitude suddenly shifts to a higher value during the onset of the storm. In most of the previous major storm studies, FACs were mainly investigated in association with high latitude dynamics, especially to capture the spatiotemporal evolutions of plasma during different phases of the storm. In a case study of the December 2015 storm, a sudden increase in FACs triggered daytime equatorward TID activity over the European region (Cherniak & Zakharenkova, 2018). A study on FACs using CHAMP during the November 2003 storm showed that dayside current densities are on average 2.5 times larger in the Southern (summer) Hemisphere than in the Northern (winter) Hemisphere (Wang et al., 2006). In our cases, we notice northern integrated FACs are ∼4 MA times higher than southern currents during the June and July 2012 storms. In the case of the December 2015 storm, southern FACs are ∼3 MA times higher than northern currents. On the other hand, the currents fluctuate during the March 2015 storm. Since the magnitudes of the net FACs for the specific hemisphere depend on ionospheric horizontal closing currents, which in turn depend on underlying ionospheric conductivity, our results indicate that the summer hemispheric high conductive ionosphere possibly induces high FACs in the summer hemisphere during storms, which in turn results in large scales of N_e depletions in the high latitudes.

Although global-scale hemispheric asymmetrical studies are limited, regional studies on geomagnetic storm morphology indicate pronounced strong seasonal effects on N_e enhancements and depressions. A statistical study on geomagnetic storms at two geophysical equivalent midlatitude locations, Wallops Island (VA) and Hobart (Tasmania), using ∼200 storm events, Mendillo and Narvaez (2010) noticed very similar enhancements and depressions at both locations on ionosonde F2-layer maximums, especially during the respective summer months. Similar studies using a group of ground-based GNSS receivers in the Northern and Southern Hemispheres also provide evidence for pronounced TEC depressions during the respective summer months (Adebiyi et al., 2014). On the other hand, a study of the March 2015 storm using Geostationary Earth Orbit (GEO) observations of the BeiDou Navigation Satellite System (BDS) showed TEC enhancements during the main phase and quasi-symmetrical TEC depressions in the recovery phase in both hemispheres (Jin et al., 2017). Our results are consistent with these results.

Although the exact physical mechanisms producing hemispheric asymmetry are not well understood, the negative phase is presumed to be mainly caused by composition changes, especially a decrease in the atomic oxygen to molecular nitrogen (O/N_2) density ratio. During geomagnetic storms, a significant level of Joule heating is possible at high latitudes due to the increased level of currents and precipitating particles. This increase in Joule heating not only increases the recombination rates but also causes upwelling of molecular species. Previously, Prölss (1997) showed a decrease in the column integrated O/N_2 density ratio due to the possible upwelling of molecular species, and the GUVI instrument on the TIMED satellite subsequently captured a decrease in the

O/N_2 density ratio during geomagnetic storms (Meier et al., 2005). Since the electron concentration in the F2 layer is directly proportional to the O/N_2 density ratio, the decrease in the oxygen density will decrease the production of ionization, and an increase in the molecular nitrogen density will increase the loss of ionization; thus, both changes combine to reduce the ionization density (Prölss, 2011). The meridional neutral wind from the summer to the winter hemisphere promotes favorable penetration of the depleted O/N_2 to the middle and low latitudes (e.g., Balan et al., 2011; Danilov, 2013). We checked the GUVI O/N_2 density ratio during the four geomagnetic storms that we investigate here and found that their values show good agreement with our TEC depletion structures. This result further supports the aforementioned theorized link between N_e and depleted O/N_2. In recent studies, researchers have also argued that additional factors, such as TID activity and vertical drift, also contribute to regional N_e or TEC depressions during storms (e.g., Ercha et al., 2019; Wang et al., 2021).

6. Conclusions

We investigated global large-scale ionospheric N_e responses during four selected geomagnetic storms using space-based and ground-based TEC and N_e measurements. Two of the selected storms occurred during boreal summer (June and July 2012), one storm occurred during austral summer (December 2015), and the other occurred during the equinoctial month (March 2015). We utilized space-based topside TEC measurements from onboard POD GNSS receivers in the COSMIC-1 (>800 km), GRACE (>450 km), and MetOp-A/B (>830 km) missions, as well as N_e retrieval profiles from GNSS-RO receivers onboard COSMIC-1 and GRACE. We also utilized ground-based VTEC measurements from a large number of GNSS receivers in a global network. After a careful analysis of global measurement patterns, we estimated latitude-time time series using zonal means, averaged based on satellite orbital times in the case of space-based data and averaged hourly for ground-based data. The daytime TEC and N_e time series were analyzed for different phase periods of the four geomagnetic storms.

We found that the interhemispheric spatiotemporal changes in TEC show good agreement between space-based and ground-based observations for all four geomagnetic storms. The results also show good agreement with the established global 3D view obtained using GNSS-RO N_e measurements. During the initial and main phases of the storm when the CME energy arrives at auroral latitudes, the global 3D daytime view captures large-scale storm-induced N_e enhancements and uplifting at high latitudes. A time delay is also evident in daytime N_e enhancements and uplifting between summer and winter high latitudes for the two boreal summer storms. While the observed feature shows good agreement with space-based and ground-based TEC observations, this result was not verified in the other two storms since a sufficient number of GNSS-RO N_e profiles are unavailable. Subsequently, depletions in N_e and TEC occur at high latitudes and start progressing into midlatitude and low latitude as the storm reaches its recovery phase. For June and July 2012 (boreal summer) storms, enhanced depletions occurred in the Northern Hemisphere. During the recovery phase, the mean TEC values at 60°N magnetic latitude are decreased by ∼50% in the case of GRACE and by ∼65% in the case of ground observations. These changes are not evident in the conjugate 60°S magnetic latitude. On the other hand, this process is reversed during the recovery phase of the December 2015 (austral summer) storm. This pattern is not evident in the March 2015 storm. Instead, it was a quasi-symmetrical response. The observed patterns have even become prominent in the TEC perturbation analysis. A similar effect is also observed during nighttime.

The AMPERE measurements recorded during these storms indicate that the integrated daytime FACs in the polar latitudes are higher in the summer hemisphere than in the winter hemisphere. Although slightly more FACs flow in the summer hemisphere than in the winter hemisphere, this difference in magnitude suddenly increases during the onset of the storm. In the case of the June and July 2012 storms (boreal summer), the integrated FACs in the north are ∼4 MA higher than those in the south. In the case of the December 2015 storm (austral summer), the integrated FACs in the south are ∼3 MA higher than those in the north. On the other hand, a fluctuating nature in the integrated FACs appears between north and south during the March 2015 storm (equinoctial month). The observed interhemispheric large-scale TEC and N_e responses during the storms suggest that summer preconditioning in the ionosphere-thermosphere system plays an important role in the ionospheric responses. This hypothesis is supported by the observed sudden increase in FACs in the summer hemisphere during the onset of the storms. An increased level of currents in the summer hemisphere at high latitudes and the subsequent increase in Joule heating might further influence the decrease in the O/N_2 density ratio and cause N_e depletions. The meridional summer-to-winter wind facilitates the penetration of the depleted O/N_2 density ratio to the middle and low latitudes and hence the interhemispheric asymmetry.

Data Availability Statement

The authors would like to acknowledge UCAR/CDAAC services for processing and distributing space-based GNSS TEC and GNSS-RO data (acquired from https://cdaac-www.cosmic.ucar.edu), MIT Haystack Observatory and CEDAR for ground-based GNSS data (acquired through http://cedar.openmadrigal.org), Johns Hopkins/APL for AMPERE data (acquired from http://ampere.jhuapl.edu), and Kyoto University/WDC (http://wdc.kugi.kyoto-u.ac.jp) and IAGA/ISGI (http://isgi.unistra.fr) for geomagnetic data.

Acknowledgments

The work was supported by the NASA's Sun-Climate Research at Goddard Space Flight Center (GSFC) and the Living with a Star Program. The authors also thank the reviewers whose comments and suggestions helped to improve the quality of this manuscript.

References

Abdu, M. A., Batista, I. S., Bertoni, F., Reinisch, B. W., Kherani, E. A., & Sobral, J. H. A. (2012). Equatorial ionosphere responses to two magnetic storms of moderate intensity from conjugate point observations in Brazil. *Journal of Geophysical Research*, *117*, A05321. https://doi.org/10.1029/2011JA017174

Adebiyi, S. J., Adimula, I. A., & Oladipo, O. A. (2014). Seasonal variations of GPS derived TEC at three different latitudes of the southern hemisphere during geomagnetic storms. *Advances in Space Research*, *53*(8), 1246–1254. doi https://doi.org/10.1016/j.asr.2014.01.028

Allen, J. H., & Kroehl, H. W. (1975). Spatial and temporal distributions of magnetic effects of auroral electrojets as derived from AE indices. *Geophysical Research Letters*, *80*(25), 3667–3677. https://doi.org/10.1029/JA080i025p03667

Amory-Mazaudier, C., Bolaji, O. S., & Doumbia, V. (2017). On the historical origins of the CEJ, DP2, and Ddyn current systems and their roles in the predictions of ionospheric responses to geomagnetic storms at equatorial latitudes. *Journal of Geophysical Research: Space Physics*, *122*, 7827–7833. https://doi.org/10.1002/2017JA024132

Anderson, B. J., Korth, H., Waters, C. L., Green, D. L., Merkin, V. G., Barnes, R. J., & Dyrud, L. P. (2014). Development of large-scale Birkeland currents determined from the active magnetosphere and planetary electrodynamics response experiment. *Geophysical Research Letters*, *41*, 3017–3025. https://doi.org/10.1002/2014GL059941

Anderson, B. J., Takahashi, K., & Toth, B. A. (2000). Sensing global Birkeland currents with iridium® engineering magnetometer data. *Geophysical Research Letters*, *27*(24), 4045–4048. https://doi.org/10.1029/2000GL000094

Astafyeva, E. (2009). Dayside ionospheric uplift during strong geomagnetic storms as detected by the CHAMP, SAC-C, TOPEX and Jason-1 satellites. *Advances in Space Research*, *43*(11), 1749–1756. https://doi.org/10.1016/j.asr.2008.09.036

Astafyeva, E., Zakharenkova, I., & Förster, M. (2015). Ionospheric response to the 2015 St. Patrick's Day storm: A global multi-instrumental overview. *Journal of Geophysical Research: Space Physics*, *120*, 9023–9037. https://doi.org/10.1002/2015JA021629

Balan, N., Bailey, G. J., Moffett, R. J., Su, Y. Z., & Titheridge, J. E. (1995). Modelling studies of the conjugate-hemisphere differences in ionospheric ionization at equatorial anomaly latitudes. *Journal of Atmospheric and Terrestrial Physics*, *57*, 279–292. https://doi.org/10.1016/0021-9169(94)E0019-J

Balan, N., Souza, J., & Bailey, G. J. (2018). Recent developments in the understanding of equatorial ionization anomaly: A review. *Journal of Atmospheric and Solar-Terrestrial Physics*, *171*, 3–11. https://doi.org/10.1016/j.jastp.2017.06.020

Balan, N., Yamamoto, M., Liu, J. Y., Otsuka, Y., Liu, H., & Lühr, H. (2011). New aspects of thermospheric and ionospheric storms revealed by CHAMP. *Journal of Geophysical Research*, *116*, A07305. https://doi.org/10.1029/2010JA016399

Balthazor, R. L., & Moffett, R. J. (1997). A study of atmospheric gravity waves and travelling ionospheric disturbances at equatorial latitudes. *Annales Geophysicae*, *15*(8), 1048–1056. https://doi.org/10.1007/s00585-997-1048-4

Belehaki, A., Jakowski, N., & Reinisch, B. W. (2004). Plasmaspheric electron content derived from GPS TEC and digisonde ionograms. *Advances in Space Research*, *33*(6), 833–837. https://doi.org/10.1016/j.asr.2003.07.008

Bruinsma, S., Forbes, J. M., Nerem, R. S., & Zhang, X. (2006). Thermosphere density response to the 20-21 November 2003 solar and geomagnetic storm from CHAMP and GRACE accelerometer data. *Journal of Geophysical Research*, *111*, A06303. https://doi.org/10.1029/2005JA011284

Cherniak, I., & Zakharenkova, I. (2018). Large-scale traveling ionospheric disturbances origin and propagation: Case study of the December 2015 geomagnetic storm. *Space Weather*, *16*, 1377–1395. https://doi.org/10.1029/2018SW001869

Cherniak, I. V., Zakharenkova, I. E., Krankowski, A., & Shagimuratov, I. I. (2012). Plasmaspheric electron content derived from GPS TEC and FORMOSAT-3/COSMIC measurements: Solar minimum condition. *Advances in Space Research*, *50*(4), 427–440. https://doi.org/10.1016/j.asr.2012.04.002

Coster, A., & Foster, J. C. (2007). Space-weather impacts of the sub-auroral polarization stream. *URSI Radio Science Bulletin*, *2007*(321), 28–36. https://ieeexplore.ieee.org/document/7909676

Coster, A., Goncharenko, L., Zhang, S.-R., Erickson, P. J., Rideout, W., & Vierinen, J. (2017). GNSS observations of ionospheric variations during the 21 August 2017 Solar Eclipse. *Geophysical Research Letters*, *44*, 12041–12048. https://doi.org/10.1002/2017GL075774

Coster, A., & Skone, S. (2009). Monitoring storm-enhanced density using IGS reference station data. *Journal of Geodesy*, *83*(3–4), 345–351. https://doi.org/10.1007/s00190-008-0272-3

Coxon, J. C., Milan, S. E., Carter, J. A., Clausen, L. B. N., Anderson, B. J., & Korth, H. (2016). Seasonal and diurnal variations in AMPERE observations of the Birkeland currents compared to modeled results. *Journal of Geophysical Research: Space Physics*, *121*, 4027–4040. https://doi.org/10.1002/2015JA022050

Danilov, A. D. (2013). Ionospheric F-region response to geomagnetic disturbances. *Advances in Space Research*, *52*(3), 343–366. https://doi.org/10.1016/j.asr.2013.04.019

Dashora, N., Suresh, S., & Niranjan, K. (2019). Interhemispheric asymmetry in response of low-latitude ionosphere to perturbation electric fields in the main phase of geomagnetic storms. *Journal of Geophysical Research: Space Physics*, *124*, 7256–7282. https://doi.org/10.1029/2019JA026671

Duncan, R. A. (1969). F-region seasonal and magnetic-storm behaviour. *Journal of Atmospheric and Terrestrial Physics*, *31*, 59–70. https://doi.org/10.1016/0021-9169(69)90081-6

Ercha, A., Zou, S., Ridley, A., Zhang, S., Coster, A., Erickson, P. J., et al. (2019). Merging of storm time midlatitude traveling ionospheric disturbances and equatorial plasma bubbles. *Space Weather*, *17*, 285–298. https://doi.org/10.1029/2018SW002101

Fejer, B. G., Larsen, M. F., & Farley, D. T. (1983). Equatorial disturbance dynamo electric fields. *Geophysical Research Letters*, *10*(7), 537–540. https://doi.org/10.1029/GL010i007p00537

Förster, M., & Jakowski, N. (2000). Geomagnetic storm effects on the topside ionosphere and plasmasphere: A compact tutorial and new results. *Surveys in Geophysics*, *21*(1), 47–87. https://doi.org/10.1023/A:1006775125220

Foster, J. C. (1993). Storm time plasma transport at middle and high latitudes. *Journal of Geophysical Research*, *98*(A2), 1675–1689. https://doi.org/10.1029/92JA02032

Foster, J. C., & Burke, W. J. (2002). Saps: A new categorization for sub-auroral electric fields. *Eos, Transactions American Geophysical Union*, *83*(36), 393. https://doi.org/10.1029/2002EO000289

Foster, J. C., & Vo, H. B. (2002). Average characteristics and activity dependence of the subauroral polarization stream. *Journal of Geophysical Research*, *107*(A12), 1475. https://doi.org/10.1029/2002JA009409

Fujii, R., Iijima, T., Potemra, T. A., & Sugiura, M. (1981). Seasonal dependence of large-scale Birkeland currents. *Geophysical Research Letters*, *8*(10), 1103–1106. https://doi.org/10.1029/GL008i010p01103

Fuller-Rowell, T. J., Codrescu, M. V., Roble, R. G., & Richmond, A. D. (1997). How does the thermosphere and ionosphere react to a geomagnetic storm? *American Geophysical Union Geophysical Monograph Series*, *98*, 203–225. https://doi.org/10.1029/GM098p0203

Gonzalez, W. D., Joselyn, J. A., Kamide, Y., Kroehl, H. W., Rostoker, G., Tsurutani, B. T., & Vasyliunas, V. M. (1994). What is a geomagnetic storm? *Journal of Geophysical Research*, *99*(A4), 5771–5792. https://doi.org/10.1029/93JA02867

Gopalswamy, N. (2010). The CME link to geomagnetic storms. In A. G.Kosovichev, A. H.Andrei, & J.-P.Rozelot (Eds.), *Solar and stellar variability: Impact on Earth and Planets* (Vol. 264, p. 326–335). https://doi.org/10.1017/S1743921309992870

Gopalswamy, N., Akiyama, S., & Yashiro, S. (2020). The state of the heliosphere revealed by limb-halo coronal mass ejections in solar cycles 23 and 24. *The Astrophysical Journal Letters*, *897*(1), L1. https://doi.org/10.3847/2041-8213/ab9b7b

Gopalswamy, N., Akiyama, S., Yashiro, S., & Xie, H. (2018). Coronal flux ropes and their interplanetary counterparts. *Journal of Atmospheric and Solar-Terrestrial Physics*, *180*, 35–45. https://doi.org/10.1016/j.jastp.2017.06.004

Gopalswamy, N., Tsurutani, B., & Yan, Y. (2015). Short-term variability of the Sun-Earth system: An overview of progress made during the CAWSES-II period. *Progress in Earth and Planetary Science*, *2*, 13. https://doi.org/10.1186/s40645-015-0043-8

Gopalswamy, N., Yashiro, S., Xie, H., Akiyama, S., & Mäkelä, P. (2015). Properties and geoeffectiveness of magnetic clouds during solar cycles 23 and 24. *Journal of Geophysical Research: Space Physics*, *120*, 9221–9245. https://doi.org/10.1002/2015JA021446

Greenspan, M. E., Rasmussen, C. E., Burke, W. J., & Abdu, M. A. (1991). Equatorial density depletions observed at 840 km during the great magnetic storm of March 1989. *Journal of Geophysical Research*, *96*(A8), 13931–13942. https://doi.org/10.1029/91JA01264

Heelis, R. A., Sojka, J. J., David, M., & Schunk, R. W. (2009). Storm time density enhancements in the middle-latitude dayside ionosphere. *Journal of Geophysical Research*, *114*, A03315. https://doi.org/10.1029/2008JA013690

Hess, P., & Zhang, J. (2014). Stereoscopic study of the kinematic evolution of a coronal mass ejection and its driven shock from the sun to the Earth and the prediction of their arrival times. *The Astrophysical Journal*, *792*(1), 49. https://doi.org/10.1088/0004-637X/792/1/49

Horvath, I., & Crozier, S. (2007). Software developed for obtaining GPS-derived total electron content values. *Radio Science*, *42*, RS2002. https://doi.org/10.1029/2006RS003452

Horvath, I., & Lovell, B. C. (2015). Positive and negative ionospheric storms occurring during the 15 May 2005 geomagnetic superstorm. *Journal of Geophysical Research: Space Physics*, *120*, 7822–7837. https://doi.org/10.1002/2015JA021206

Hunsucker, R. D. (1982). Atmospheric gravity waves generated in the high-latitude ionosphere: A review (Paper 1R1822). *Reviews of Geophysics and Space Physics*, *20*(2), 293–315. https://doi.org/10.1029/RG020i002p00293

Immel, T. J., & Mannucci, A. J. (2013). Ionospheric redistribution during geomagnetic storms. *Journal of Geophysical Research: Space Physics*, *118*, 7928–7939. https://doi.org/10.1002/2013JA018919

Jin, S., Jin, R., & Kutoglu, H. (2017). Positive and negative ionospheric responses to the March 2015 geomagnetic storm from BDS observations. *Journal of Geodesy*, *91*(6), 613–626. https://doi.org/10.1007/s00190-016-0988-4

Klimenko, M. V., & Klimenko, V. V. (2012). Disturbance dynamo, prompt penetration electric field and overshielding in the Earth's ionosphere during geomagnetic storm. *Journal of Atmospheric and Solar-Terrestrial Physics*, *90*, 146–155. https://doi.org/10.1016/j.jastp.2012.02.018

Klobuchar, J. A. (1996). Ionospheric effects on GPS. In B. W.Parkinson, & J. J.Spilker (Eds.), *Global positioning system: Theory and applications. Advances in Space Research* (Vol. 1). New York, NY: American Institute of Aeronautics and Astronautics.

Kuai, J., Liu, L., Lei, J., Liu, J., Zhao, B., Chen, Y., et al. (2017). Regional differences of the ionospheric response to the July 2012 geomagnetic storm. *Journal of Geophysical Research: Space Physics*, *122*, 4654–4668. https://doi.org/10.1002/2016JA023844

Lanyi, G. E., & Roth, T. (1988). A comparison of mapped and measured total ionospheric electron content using global positioning system and beacon satellite observations. *Radio Science*, *23*(4), 483–492. https://doi.org/10.1029/RS023i004p00483

Lear, W. (1987). *GPS navigation for low-Earth orbiting vehicles (NASA 87-FM-2, Rev. 1, JSC-32031, 1)*. Houston, TX: Lyndon B. Johnson Space Center.

Liu, J., Liu, L., Nakamura, T., Zhao, B., Ning, B., & Yoshikawa, A. (2014). A case study of ionospheric storm effects during long-lasting southward IMF B_z-driven geomagnetic storm. *Journal of Geophysical Research: Space Physics*, *119*, 7716–7731. https://doi.org/10.1002/2014JA020273

Liu, J. Y., Lin, C. Y., Lin, C. H., Tsai, H. F., Solomon, S. C., Sun, Y. Y., et al. (2010). Artificial plasma cave in the low-latitude ionosphere results from the radio occultation inversion of the FORMOSAT-3/COSMIC. *Journal of Geophysical Research*, *115*, A07319. https://doi.org/10.1029/2009JA015079

Lu, G., Goncharenko, L., Nicolls, M. J., Maute, A., Coster, A., & Paxton, L. J. (2012). Ionospheric and thermospheric variations associated with prompt penetration electric fields. *Journal of Geophysical Research*, *117*, A08312. https://doi.org/10.1029/2012JA017769

Lu, G., Goncharenko, L. P., Richmond, A. D., Roble, R. G., & Aponte, N. (2008). A dayside ionospheric positive storm phase driven by neutral winds. *Journal of Geophysical Research*, *113*, A08304. https://doi.org/10.1029/2007JA012895

Maeda, H., Sakurai, K., Ondoh, T., & Yamamoto, M. (1962). A study of solar-terrestrial relationships during the IGY and IGC. *Annales de Geophysique*, *18*, 305.

Mannucci, A. J., Tsurutani, B. T., Iijima, B. A., Komjathy, A., Saito, A., Gonzalez, W. D., et al. (2005). Dayside global ionospheric response to the major interplanetary events of October 29-30, 2003 "Halloween Storms". *Geophysical Research Letters*, *32*, L12S02. https://doi.org/10.1029/2004GL021467

Mannucci, A. J., Wilson, B. D., Yuan, D. N., Ho, C. H., Lindqwister, U. J., & Runge, T. F. (1998). A global mapping technique for GPS-derived ionospheric total electron content measurements. *Radio Science*, *33*(3), 565–582. https://doi.org/10.1029/97RS02707

Maruyama, N., Sazykin, S., Spiro, R. W., Anderson, D., Anghel, A., Wolf, R. A., et al. (2007). Modeling storm-time electrodynamics of the low-latitude ionosphere thermosphere system: Can long lasting disturbance electric fields be accounted for? *Journal of Atmospheric and Solar-Terrestrial Physics*, *69*(10–11), 1182–1199. https://doi.org/10.1016/j.jastp.2006.08.020

Meier, R. R., Crowley, G., Strickland, D. J., Christensen, A. B., Paxton, L. J., Morrison, D., & Hackert, C. L. (2005). First look at the 20 November 2003 superstorm with TIMED/GUVI: Comparisons with a thermospheric global circulation model. *Journal of Geophysical Research*, *110*, A09S41. https://doi.org/10.1029/2004JA010990

Mendillo, M. (1973). A study of the relationship between geo-magnetic storms and ionospheric disturbances at mid-latitudes. *Planetary and Space Science*, *21*(3), 349–358. https://doi.org/10.1016/0032-0633(73)90033-0

Mendillo, M. (2006). Storms in the ionosphere: Patterns and processes for total electron content. *Reviews of Geophysics*, *44*, RG4001. https://doi.org/10.1029/2005RG000193

Mendillo, M., & Narvaez, C. (2010). Ionospheric storms at geophysically-equivalent sites—Part 2: Local time storm patterns for sub-auroral ionospheres. *Annales Geophysicae*, *28*(7), 1449–1462. https://doi.org/10.5194/angeo-28-1449-2010

Nicolls, M. J., Rodrigues, F. S., Bust, G. S., & Chau, J. L. (2009). Estimating E region density profiles from radio occultation measurements assisted by IDA4D. *Journal of Geophysical Research*, *114*, A10316. https://doi.org/10.1029/2009JA014399

Pedatella, N. M., Forbes, J. M., Maute, A., Richmond, A. D., Fang, T. W., Larson, K. M., & Millward, G. (2011). Longitudinal variations in the F region ionosphere and the topside ionosphere-plasmasphere: Observations and model simulations. *Journal of Geophysical Research*, *116*, A12309. https://doi.org/10.1029/2011JA016600

Pedatella, N. M., Yue, X., & Schreiner, W. S. (2015). An improved inversion for FORMOSAT-3/COSMIC ionosphere electron density profiles. *Journal of Geophysical Research: Space Physics*, *120*, 8942–8953. https://doi.org/10.1002/2015JA021704

Pfaff, R. F. (2012). The near-Earth plasma environment. *Space Science Reviews*, *168*(1–4), 23–112. https://doi.org/10.1007/s11214-012-9872-6

Polekh, N., Zolotukhina, N., Kurkin, V., Zherebtsov, G., Shi, J., Wang, G., & Wang, Z. (2017). Dynamics of ionospheric disturbances during the 17-19 March 2015 geomagnetic storm over East Asia. *Advances in Space Research*, *60*(11), 2464–2476. https://doi.org/10.1016/j.asr.2017.09.030

Prölss, G. W. (1997). Magnetic storm associated perturbations of the upper atmosphere. *American Geophysical Union Geophysical Monograph Series*, *98*, 227–241. https://doi.org/10.1029/GM098p0227

Prölss, G. W. (2011). Density perturbations in the upper atmosphere caused by the dissipation of solar wind energy. *Surveys in Geophysics*, *32*(2), 101–195. https://doi.org/10.1007/s10712-010-9104-0

Richmond, A. D., & Matsushita, S. (1975). Thermospheric response to a magnetic substorm. *Journal of Geophysical Research*, *80*(19), 2839–2850. https://doi.org/10.1029/JA080i019p02839

Rideout, W., & Coster, A. (2006). Automated GPS processing for global total electron content data. *GPS Solutions*, *123*(6), 219–228. https://doi.org/10.1007/s10291-006-0029-5

Ridley, A. J., & Liemohn, M. W. (2002). A model-derived storm time asymmetric ring current driven electric field description. *Journal of Geophysical Research*, *107*(A8), 1151. https://doi.org/10.1029/2001JA000051

Rostoker, G. (1996). Phenomenology and physics of magnetospheric substorms. *Journal of Geophysical Research*, *101*(A6), 12955–12973. https://doi.org/10.1029/96JA00127

Schreiner, W. S., Sokolovskiy, S. V., Rocken, C., & Hunt, D. C. (1999). Analysis and validation of GPS/MET radio occultation data in the ionosphere. *Radio Science*, *34*(4), 949–966. https://doi.org/10.1029/1999RS900034

Shinbori, A., Otsuka, Y., Sori, T., Tsugawa, T., & Nishioka, M. (2020). Temporal and spatial variations of total electron content enhancements during a geomagnetic storm on 27 and 28 September 2017. *Journal of Geophysical Research: Space Physics*, *125*, e2019JA026873. https://doi.org/10.1029/2019JA026873

Spiro, R. W., Wolf, R. A., & Fejer, B. G. (1988). Penetrating of high-latitude-electric-field effects to low latitudes during SUNDIAL 1984. *Annales Geophysicae*, *6*, 39–49.

Srivastava, N., Mishra, W., & Chakrabarty, D. (2018). Interplanetary and geomagnetic consequences of interacting CMEs of 13–14 June 2012. *Solar Physics*, *293*(1), 5. https://doi.org/10.1007/s11207-017-1227-8

Sugiura, M. (1964). Hourly values of equatorial Dst for the IGY. *Annals of the International Geophysical Year*, *1*, 35.

Sugiura, M., & Potemra, T. A. (1978). Seasonal variation in the field-aligned current as observed by Triad. *Eos, Transactions American Geophysical Union*, *59*(11), 1170.

Swarnalingam, N., Wu, D., & Themens, D. R. (2020). Comparison and evaluation of a bottom-up GPS-RO electron density retrieval for D and E regions using radar observations and models. *Journal of Atmospheric and Solar-Terrestrial Physics*, *207*, 105333. https://doi.org/10.1016/j.jastp.2020.105333

Tsurutani, B., Gonzalez, W. D., Gonzalez, A. L. C., Guarnieri, F. L., Gopalswamy, N., Grande, M., et al. (2006). Corotating solar wind streams and recurrent geomagnetic activity: A review. *Journal of Geophysical Research*, *111*, A07S01. https://doi.org/10.1029/2005JA011273

Tsurutani, B., Mannucci, A., Iijima, B., Abdu, M. A., Sobral, J. H. A., Gonzalez, W., et al. (2004). Global dayside ionospheric uplift and enhancement associated with interplanetary electric fields. *Journal of Geophysical Research*, *109*, A08302. https://doi.org/10.1029/2003JA010342

Vierinen, J., Coster, A., Rideout, W. C., Erickson, P. J., & Norberg, J. (2016). Statistical framework for estimating GNSS bias. *Atmospheric Measurement Techniques*, *9*(3), 1303–1312. https://doi.org/10.5194/amt-9-1303-2016

Wang, H., Lühr, H., Ma, S. Y., Weygand, J., Skoug, R. M., & Yin, F. (2006). Field-aligned currents observed by CHAMP during the intense 2003 geomagnetic storm events. *Annales Geophysicae*, *24*(1), 311–324. https://doi.org/10.5194/angeo-24-311-2006

Wang, Z., Zou, S., Coppeans, T., Ren, J., Ridley, A., & Gombosi, T. (2019). Segmentation of SED by boundary flows associated with westward drifting partial ring current. *Geophysical Research Letters*, *46*, 7920–7928. https://doi.org/10.1029/2019GL084041

Wang, Z., Zou, S., Liu, L., Ren, J., & Aa, E. (2021). Hemispheric asymmetries in the mid-latitude ionosphere during the September 7-8, 2017 storm: Multi-instrument observations. *Journal of Geophysical Research: Space Physics*, *126*, e2020JA028829. https://doi.org/10.1029/2020JA028829

Wu, C.-C., Liou, K., Lepping, R. P., Hutting, L., Plunkett, S., Howard, R. A., & Socker, D. (2016). The first super geomagnetic storm of solar cycle 24: "The St. Patrick's Day event (17 March 2015)". *Earth, Planets, and Space*, *68*(1), 151. https://doi.org/10.1186/s40623-016-0525-y

Wu, D. L. (2018). New global electron density observations from GPS-RO in the D- and E-Region ionosphere. *Journal of Atmospheric and Solar-Terrestrial Physics*, *171*, 36–59. https://doi.org/10.1016/j.jastp.2017.07.013

Yizengaw, E., Moldwin, M. B., Galvan, D., Iijima, B. A., Komjathy, A., & Mannucci, A. J. (2008). Global plasmaspheric TEC and its relative contribution to GPS TEC. *Journal of Atmospheric and Solar-Terrestrial Physics*, *70*(11–12), 1541–1548. https://doi.org/10.1016/j.jastp.2008.04.022

Yizengaw, E., Moldwin, M. B., Komjathy, A., & Mannucci, A. J. (2006). Unusual topside ionospheric density response to the November 2003 superstorm. *Journal of Geophysical Research*, *111*(A2), A02308. https://doi.org/10.1029/2005JA011433

Yue, X., Schreiner, W. S., Lei, J., Sokolovskiy, S. V., Rocken, C., Hunt, D. C., & Kuo, Y. H. (2010). Error analysis of Abel retrieved electron density profiles from radio occultation measurements. *Annales Geophysicae*, *28*(1), 217–222. https://doi.org/10.5194/angeo-28-217-2010

Zhang, J., Liemohn, M. W., de Zeeuw, D. L., Borovsky, J. E., Ridley, A. J., Toth, G., et al. (2007). Understanding storm-time ring current development through data-model comparisons of a moderate storm. *Journal of Geophysical Research*, *112*, A04208. https://doi.org/10.1029/2006JA011846

Zhang, S.-R., Zhang, Y., Wang, W., & Verkhoglyadova, O. P. (2017). Geospace system responses to the St. Patrick's Day storms in 2013 and 2015. *Journal of Geophysical Research: Space Physics*, *122*, 6901–6906. https://doi.org/10.1002/2017JA024232

Zhong, J., Lei, J., Dou, X., & Yue, X. (2016). Assessment of vertical TEC mapping functions for space-based GNSS observations. *GPS Solutions*, *20*, 353–362. https://doi.org/10.1007/s10291-015-0444-6

Zou, S., Moldwin, M. B., Ridley, A. J., Nicolls, M. J., Coster, A., Thomas, E. G., & Ruohoniemi, J. M. (2014). On the generation/decay of the storm-enhanced density plumes: Role of the convection flow and field-aligned ion flow. *Journal of Geophysical Research: Space Physics*, *119*, 8543–8559. https://doi.org/10.1002/2014JA020408